Climatology of near-surface wind speed from observational, reanalysis and high-resolution regional climate model data over the Tibetan Plateau

Lorenzo Minola[1,2,3] · Gangfeng Zhang[4,5,6] · Tinghai Ou[1] · Julia Kukulies[1] · Julia Curio[1] · Jose A. Guijarro[7] · Kaiqiang Deng[8] · Cesar Azorin-Molina[3] · Cheng Shen[1] · Alessandro Pezzoli[2] · Deliang Chen[1]

Abstract

As near-surface wind speed plays a role in regulating surface evaporation and thus the hydrological cycle, it is crucial to explore its spatio-temporal characteristics. However, in-situ measurements are scarce over the Tibetan Plateau, limiting the understanding of wind speed climate across this high-elevation region. This study explores the climatology of near-surface wind speed over the Tibetan Plateau by using for the first time homogenized observations together with reanalysis products and regional climate model simulations. Measuring stations across the center and the west of the plateau are at higher elevations and display higher mean and standard deviation, confirming that wind speed increases with increasing altitude. By exploring wind characteristics with a focus on seasonal cycle through cluster analysis, three regions of distinct wind regimes can be identified: (1) the central Tibetan Plateau, characterized by high elevation; (2) the eastern and the peripheral areas of the plateau; and (3) the Qaidam basin, a topographic depression strongly influenced by the blocking effect of the surrounding mountainous terrain. Notably, the ERA5 reanalysis, with its improvements in horizontal, vertical, and temporal spacing, model physics and data assimilation, demonstrates closer agreement to the measured wind conditions than its predecessor ERA-Interim. It successfully reproduces the three identified wind regimes. However, the newest ERA5-Land product does not show improvements compared to ERA5, most likely because they share most of the parametrizations. Furthermore, the two dynamical downscalings of ERA5 analyzed here fail to capture the observed wind statistics and exhibit notable biases and discrepancies also when investigating the diurnal variations. Consequently, these high-resolution downscaling products do not show add value in reproducing the observed climatology of wind speed compared to ERA5 over the Tibetan Plateau.

Keywords Wind speed · Climatology · ECMWF reanalysis · WRF downscaling · Tibetan Plateau

✉ Lorenzo Minola
lorenzo.minola@gu.se

1. Regional Climate Group, Department of Earth Sciences, University of Gothenburg, Gothenburg, Sweden

2. Interuniversity Department of Regional and Urban Studies and Planning (DIST), Politecnico and University of Turin, Turin, Italy

3. Centro de Investigaciones Sobre Desertificación, Climate, Atmosphere and Ocean Laboratory (Climatoc-Lab), Consejo Superior de Investigaciones Científicas (CIDE, CSIC-UV-Generalitat Valenciana), Moncada, Valencia, Spain

4. State Key Laboratory of Earth Surface Processes and Resource Ecology, Beijing Normal University, Beijing, China

5. Academy of Disaster Reduction and Emergency Management, Ministry of Emergency Management and Ministry of Education, Beijing Normal University, Beijing, China

6. Department of System Science, Beijing Normal University, Beijing, China

7. State Meteorological Agency (AEMET), Delegation of the Balearic Islands, Palma de Mallorca, Spain

8. School of Atmospheric Sciences, Southern Marine Science and Engineering Guangdong Laboratory (Zhuhai), Sun Yat-sen University, Zhuhai, China

1 Introduction

The Tibetan Plateau (TP), often referred to as the "Third Pole", is the highest and most extensive upland region in the world, stretching for about 1,000 km along latitude and 2,500 km along longitude, with an average elevation over 4,000 m a.s.l. (above sea level) (Yao et al. 2012). It exerts profound thermal and orographic effects on atmospheric circulation patterns on all temporal and spatial scales (Gao et al. 1981), thus playing a crucial role in influencing regional and global climate through both thermal and dynamical mechanisms (Yang et al. 2004). The TP is also referred to as the "water tower of Asia" because it is the source region of several major rivers in Asia (e.g., Yellow River, Yangtze River, and Mekong River), hence providing water resources to 1.5 billion of people in east and south Asia (Yao et al. 2012). As near-surface (i.e., 10 m above ground level) wind speed (hereafter, NSWS) can alter the surface evapotranspiration rate (e.g., by increasing the movement of air around a plant, with more saturated air close to the leaf replaced by drier air), thus driving the exchange of heat and water vapor between the surface and the atmospheric boundary layer, it partly regulates the hydrological status and controls the local water cycle (Kang et al. 2010; Yang et al. 2014; Zheng et al. 2009). In addition, with more than 60% of the TP being arid or semi-arid, NSWS is one of the key factors in shaping landforms and the geographical environment (Dong et al. 2017). For these reasons, it is crucial to understand the characteristics of climatology and variability of NSWS over the TP because of its prominent environmental implications and impacts on the water resources of 10 countries, most of them being the most densely populated countries in the world (IPCC 2019).

However, the lack of sufficient observational data limits the understanding of NSWS over the TP. In fact, compared with other terrestrial regions of the world, observations are scarce here because meteorological stations are sparsely distributed across the plateau due to its vast geographical area with complex topography, steep terrain, high elevations, and harsh environmental conditions (Ma et al. 2020). In addition, not only the density of in-situ stations is sparse, but most available stations are located in valleys (Li et al. 2018). Therefore, the sparse and biased distribution of measuring stations makes it difficult to match the high degree of landscape heterogeneity, and thus the comprehensive understanding of wind conditions across the whole TP. To overcome this challenge, more spatially-complete datasets (i.e., where data are provided on a regular longitude-latitude grid, thus able to homogeneously cover a given region), such as reanalysis products, could be used to explore NSWS characteristics of this region. In fact, by using a forecast model in which information from global observations are assimilated, reanalyses produce spatially-homogeneous data that goes several decades back in time, providing an accurate (i.e., spatially complete and physically coherent) description of the climate of the past (Dee et al. 2011). Among the most popular and used reanalysis products, we can find the ones produced over the past decades by the European Centre for Medium-Range Weather Forecasts (ECMWF), as ERA-Interim or ERA5 (see Sect. 2.2). Historical reanalyses can be used together with regional climate models to downscale information from the reanalyses and simulate more small-scale features of wind. In fact, for a region with complex terrain like the TP, topography produces strong modifications of the synoptic-scale circulation, causing high spatial variability in the near-surface flow (Whiteman 2000). Such stress of the meso- to micro-scale orographic variance is referred to as topographic drag, and its impact on the land–atmosphere momentum interaction is more prominent in mountain regions than over flat areas. Thus, models at high horizontal resolution may be needed to better represent the heterogeneity in land surface and orography, and to resolve mesoscale processes that affect wind (Jiménez et al. 2010; Li et al. 2017). Therefore, limited-domain climate model simulations with regional refinements are created by dynamically downscaling a coarser global reanalysis (AMS 2013). In particular, by downscaling the reanalysis, large-scale flow is included in the regional simulations, while regional and small-scale circulation features are generated by the regional climate model. In addition, such regional modeling with a finer resolution can improve the simulation by including topographic drags by appropriate parametrization of the subgrid orographic variance and effects (i.e., subgrid orographic drag parametrization for turbulence-scale orographic form drag; Zhou et al. 2018). In this way, dynamical downscaling products can capture more climatic information at different scales and at a higher resolution, being able to reduce local biases of reanalysis datasets, even in regions with complex topography where subgrid scale orographic variation exerts relevant turbulent form drag on atmospheric flows (Giorgi and Shields 1999; Jiménez and Dudhia 2012; Gao et al. 2015; Li et al. 2017; Ou et al. 2020). However, the improvements of dynamical downscaling over complex terrains need to be verified as insufficient representation of subgrid orography can lead to systematic biases in numerical simulations, as well as different formulations of drag induced by the unresolved subgrid orographic variance can cause large differences in simulated stresses over mountainous regions (Zhou et al. 2017). Therefore, before any reanalysis or climate model dataset can be used to study wind speed conditions in a given area, especially if characterized by complex topography, its ability in representing

observed NSWS statistics must be proven. In fact, previous studies have shown that their capability in simulating wind speed is strongly dependent on the selected region and the considered time period (Ramon et al. 2019; Wohland et al. 2019; Miao et al. 2020). For this reason, it is necessary to explore the reliability of modeled outputs by comparing them with observations, so that the skills of the models in simulating wind climate can be verified (Kunz et al. 2010). For example, several studies have shown improvements in modeling the total precipitation as well as the diurnal cycle of precipitation when going to finer scales over the TP (e.g., Lin et al. 2018; Li et al. 2021a, b). But when it comes to surface winds, these benefits have been less studied and systematically explored for different high-resolution regional model datasets.

So far, the literature has largely focused on investigating NSWS changes over the TP (e.g., You et al. 2014; Duan and Xiao 2015), but only a few studies have explored the sub-regional differences in NSWS climatology and how these are simulated by reanalyses or dynamical downscaling products (Li et al. 2017; Li et al. 2021a, b; Yao et al. 2018; Zao et al. 2019). Despite the uneven distribution of the meteorological stations over the TP, available observations can be used to investigate how wind conditions are simulated by reanalyses and climate models. Only when their reliability is verified, those simulated outputs can be employed to comprehensively investigate the NSWS climate, trends, and variability over the whole heterogeneous landscape of the TP.

For all these reasons, this study aims to: (a) improve the understanding of the spatio-temporal climatology of homogenized (i.e., variations caused by non-climatic factors have been removed – see Sect. 2.1) observed NSWS over the TP by identifying the most relevant geographical features for the NSWS climatology; (b) evaluate the performance of recent reanalyses in simulating NSWS observations; and (c) assess if dynamic downscaling of current reanalyses adds value in reproducing the observed NSWS climatology. In this study, we focus on the few recent ECMWF reanalyses (i.e., ERA-Interim, ERA5, and ERA5-Land – see Sect. 2.2) to evaluate if and how their improvements during the last decades have affected their performance in modeling NSWS over the TP. Similarly, we only look at two different downscaling products of ERA5 to identify the potential added value of downscaling compared to the downscaled reanalysis when it comes to wind simulations. In addition, it is important to highlight that this is the first study which analyses NSWS climatology over the TP using homogenized observed series, i.e. series where their changes are only caused by variations in climate and the effect of possible non-climatic factors are removed and corrected (see Sect. 2.1).

The paper is structured as follows: the data used by the study (e.g., wind observations and modeled outputs) is presented in Sect. 2. Section 3 describes the methods applied here to investigate wind climatology and it is presented how the comparison between wind measurements and modeled data is made. Section 4 shows and discusses the results of the analyses: in particular, after exploring the climatology of observed NSWS (Sect. 4.1), it is evaluated the performance of reanalysis (Sect. 4.2) and dynamical downscaling (Sect. 4.3) products in reproducing observed wind characteristics. Conclusions are drawn in Sect. 5.

2 Data

2.1 NSWS observations

Daily means of NSWS observations from 104 stations over the TP for 1960–2020 are provided by the China Meteorological Administration (CMA). Those weather stations do not cover evenly the whole TP, but are mostly located in the east, with only a few stations in the west and center of the plateau (Fig. 1). Multi-decadal NSWS series can be unrepresentative of the actual climate and its variations over time when the presence of various types of non-climatic factors, as station relocations and anemometer height and type changes can create artificial shifts (or break-points) in the observed series (Aguilar et al. 2003; Wan et al. 2010). Therefore, it is necessary to apply a homogenization protocol which is able to detect those artificial shifts and afterwards correct the biases which those inhomogeneities create. In this study, *Climatol* (Guijarro 2018) is applied to identify break-points, remove their biases, reject outliers, and infill missing data. *Climatol* is a R (R Core Team 2020) package for quality controlling, homogenizing, and missing data infilling of climate series. More info about this software can be retrieved at http://www.climatol.eu/ (last accessed 7 August 2023). *Climatol* has been widely used for homogenizing NSWS series in various studies (e.g., Azorin-Molina et al. 2019; Shi et al. 2019; Zhang et al. 2020; Minola et al. 2021a, b), proving to be a reliable tool for successfully homogenizing wind series. Here, homogenization is performed on monthly aggregates, using only nearest data available at each time step as reference for identifying break-points, rejecting outliers, and infilling of missing data. A homogenized dataset of 104 monthly mean NSWS series over the TP for 1960–2020 is thus created by the applied homogenization protocol.

To analyze the diurnal cycle of NSWS over the TP, sub-daily observations are retrieved from the Met Office Hadley Centre Integrated Surface Database (HadISD) (Smith et al. 2011; Dunn et al. 2012, 2014, 2016; Dunn 2019). In particular, this study uses the HadISD version 3.1.1 (https://www.metoffice.gov.uk/hadobs/hadisd/; last accessed 7 August 2023). The HadISD archive contains synoptic reports (sub-daily, station-based, and quality-controlled) from a large

Fig. 1 Elevation map of the study area with the location of the measuring stations selected from the CMA dataset (104 stations; blue circles) and the CMA's measuring stations with sub-daily observations available from the HadISD.3.1.1 dataset (27 stations; yellow stars)
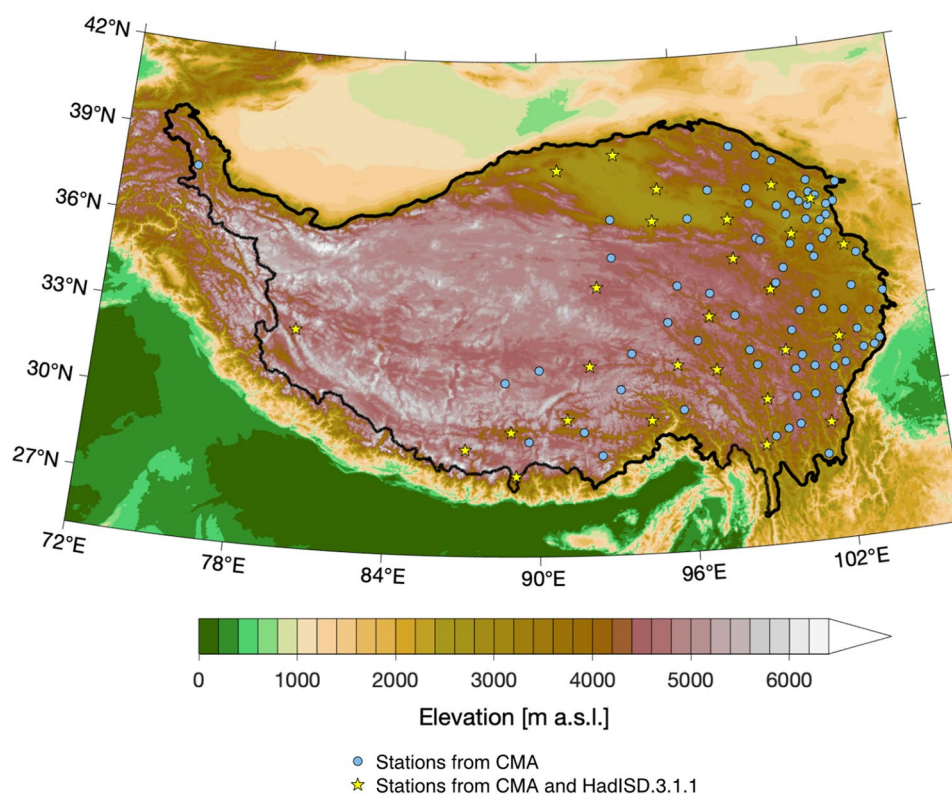
number of global measuring stations. Here, 3-hourly (i.e., at UTC 00:00, 03:00, 06:00, 09:00, etc.) measurements of mean NSWS are collected from 27 stations over the TP for 2017–2018 (Fig. 1). Those 27 stations are also included in the CMA 1960–2020 dataset previously presented. As it is not possible to apply a reliable homogenization protocol for 3-hourly series, we only focus on the recent 2017–2018 because missing and flagged (i.e., records removed by quality control flags) observed values are minimal during this time period.

2.2 Reanalyses

This study compares observed NSWS with wind outputs of three reanalysis datasets from ECMWF: (a) ERA-Interim (hereafter, ERAINT), (b) ERA5, and (c) ERA5-Land. ERA5 is the fifth generation ECMWF reanalysis, which has replaced its predecessor ERAINT (Hersbach et al. 2018). Compared to ERAINT, ERA5 benefits from 10 years of improvements in model physics and data assimilation, as well as in the increased number of ingested observations, with newly available observed datasets now assimilated. It is noteworthy to remark that in all ECMWF products near-surface wind measurements over land are excluded from the data assimilation process (Dee et al. 2011). ERA5 outputs are produced hourly at a horizontal resolution of 31 km, whereas ERAINT climate variables are available 3-hourly

at a 79 km horizontal grid-spacing (Fig. S1). ERA5-Land has been produced by replaying the land component of the ERA5 climate reanalysis through global high-resolution numerical integrations (Muñoz-Sabater et al. 2021). Even though ERA5-Land shares most of the parametrizations with ERA5, its main advantage compared to ERA5 is the horizontal resolution (Fig. S1), which is enhanced globally to 9 km (while the temporal resolution is hourly as in ERA5).

3-hourly (for ERAINT) and hourly (for ERA5 and ERA5-Land) 10-m height zonal (u) and meridional (v) wind components are downloaded for 1981–2018, which is the common time period for both observations and the three selected reanalyses. In particular, ERAINT wind data is downloaded from https://apps.ecmwf.int/datasets/data/interim-full-daily/levtype=sfc/ (last accessed 7 August 2023); ERA5 and ERA5-Land wind outputs are accessed from the Copernicus website (https://cds.climate.copernicus.eu/cdsapp#!/dataset/reanalysis-era5-single-levels?tab=overview and https://cds.climate.copernicus.eu/cdsapp#!/dataset/reanalysis-era5-land?tab=form, respectively; last accessed 7 August 2023). At each grid point, NSWS is calculated as the square root of the sum of the squared wind components at the land-surface single level at a given time:

$$NSWS = \sqrt{(u^2 + v^2)} \tag{1}$$

Once that hourly (and 3-hourly for ERAINT) NSWS series are computed using Eq. 1, monthly mean NSWS series are calculated. For evaluating the performance of the reanalyses in simulating observations, the observed NSWS series at a given measuring station is compared with the NSWS series from the closest reanalysis grid point, under the assumption that the closest grid series matches the observed one better than any other more distant grid point series (Minola et al. 2020).

2.3 Dynamical downscaling products

This study evaluates the performance in simulating NSWS of two high-resolution downscaling products, which are created by downscaling ERA5 using the regional Weather Research and Forecasting (WRF) model (Skamarock et al. 2008): (1) a WRF downscaling at a 9-km resolution (hereafter, WRF-9km), and (2) the High Asia Refined analysis version 2 (hereafter, HAR). In the WRF-9km (Ou et al. 2020, 2023; Sun et al. 2021), ERA5 has been dynamically downscaled at a 9 km resolution for East Asia with a focus on the TP region since 1979. More info about this product and data access at http://biggeo.gvc.gu.se/TPReanalysis/ (last accessed 7 August 2023). In a similar way, HAR (Maussion et al. 2011, 2014; Wang et al. 2020) is generated by dynamical downscaling ERA5 using WRF. HAR outputs are at a 10 km grid-spacing from 1980. A more detailed description of HAR and the outputs of the model can be retrieved at this link: https://www.klima.tu-berlin.de/index.php?show=daten_har2&lan=de (last accessed 7 August 2023).

These two datasets have been chosen as, among the available high-resolution regional climate models covering the TP region, they are the only dynamical downscaling products of ERA5 which have climate simulations over the TP at a horizontal grid-spacing of ~10 km for a 30-years time period (no other datasets have simulations with such high spatial resolution for such long time-period; Kukulies et al. 2023). Both datasets have largely been used to explore the climatology across this region (e.g., Curio et al. 2015; Ou et al. 2023). Even if they are both obtained by dynamical downscaling using the WRF model, with ERA5 data used as forcing data, the setup of the downscaling differs between the two products. Among the differences, e.g., WRF-9km uses the Yonsei University (YSU) Planetary Boundary Layer (PBL) scheme (Hong et al. 2006), while HAR parametrizes the PBL with the Mellor-Yamada-Janijic scheme (Janjić 1994). For the cumulus parameterization, HAR adopts the Grell 3D scheme (Grell 1993; Grell and Dévényi 2002); WRF-9km turned off the convective parameterization. To prevent the model from deviating too far from the forcing data (i.e., to constrain large-scale driving field and thus reduce the impact of model domain size on the regional

simulation), HAR uses daily re-initialization: each run started at 12:00 UTC and contained 36 h, with the first 12 h as the spin-up time. Instead, WRF-9km uses as a forcing strategy spectral nudging, which consists of adding a new term to the tendencies of the model variables that relaxes the selected part of the spectrum to the corresponding waves from driving fields (in this case, ERA5).

In the same way as hourly NSWS has been calculated for ERA5 and ERA5-Land, hourly NSWS series are created using Eq. 1 from u and v outputs of WRF-9km and HAR. Monthly mean NSWS series are then created and the closest grid point series is compared to the observed one of a given series. For comparison between observed, WRF-9km and HAR NSWS series, we use 1991–2018 which is the common time period between those datasets (in fact, while HAR outputs are continuously updated to be extended back to 1979, outputs were available only for the period after 1991 when this study was carried out).

2.4 Global digital elevation model

To explore the influence of topography on NSWS statistics, we obtain land surface elevation data from the global digital elevation model by the Earth Resources Observation and Science (EROS) Center: the Global 30 Arc-Second Elevation (GTOPO30) dataset (Gesch et al. 1999). GTOPO30 combines several raster and vector sources of topographic information to derive elevation values on a regularly-spaced grid of 30 arc seconds (approximately 1 km). GTOPO30 data is available for downloading at https://www.usgs.gov/centers/eros/science/usgs-eros-archive-digital-elevation-global-30-arc-second-elevation-gtopo30#overview (last accessed 7 August 2023).

3 Methods

3.1 Statistical measures for comparison

To quantify the agreement between observed and modeled NSWS, we use the following statistical methods: (1) Pearson's correlation coefficient, which measures the degree of association (i.e., linear relationship; Gibbons and Chakrborti 2003) and it is reported at the significant level of $p < 0.05$; (2) Root Mean Squared Error (hereafter, RMSE), which mathematically expresses the vicinity between two datasets (i.e., how far predictions fall from measured true values; Von Storch and Zwiers 1999); (3) bias, which identifies the tendency to constant deviate of a realization compared to another; and (4) coefficient of determination (hereafter, R^2), which represents the proportion of the variance for a dependent variable that is explained by an independent variable in a regression model.

## 3.2 Classification of the seasonal and diurnal cycle of NSWS

This study uses the k-means clustering method (Wilks 1995) to identify regional regimes in NSWS seasonality and diurnal variability over the plateau. By applying the k-mean clustering, the mean seasonal (diurnal) cycles of NSWS of the different stations/grid points are portioned into a given number of clusters based on the feature similarity of their seasonal (diurnal) regimes. The k-means clustering is applied to the seasonal and diurnal cycle anomalies of NSWS (i.e., normalized seasonal and diurnal cycles, where the annual and daily mean is removed from each monthly and hourly mean value, respectively). In this way, the classification focuses on the differences in shape rather than differences in overall magnitude. The number of partitions in the cluster analysis has been chosen to reach a good balance between coherent patterns and sufficient distinction between classes. The k-means clustering method, for example, has been used for the analysis of precipitation seasonality over the TP (Curio and Scherer 2016).

3.3 Time-scale for calculation of reanalyzed NSWS

As explained in Sect. 2.2, the reanalyzed NSWS is calculated from Eq. 1 using the hourly (and 3-hourly for ERAINT) u and v wind components outputted by the reanalysis. The monthly mean series of NSWS are then calculated based on those hourly NSWS series (hereafter, NSWS hourly-calculated). This process demands a lot of computational resources, as it requires that data are downloaded at high temporal resolution (i.e., hourly) for multiple years in a large spatial domain, as the one of the TP. It also requires a lot of computation power in order to perform the necessary calculation of monthly averages. A less computational-costly alternative is to download already-calculated monthly means of u and v from the ECMWF archive (where they are available), and then to calculate NSWS using Eq. 1 but with monthly-averaged zonal and meridional wind components (hereafter, NSWS monthly-calculated). Mathematically, differences must emerge when using Eq. 1 with hourly- or monthly-averaged NSWS. But the question is: how different are aggregated statistics between the NSWS hourly-calculated and the NSWS monthly-calculated? In addition, where are these differences most significant? Fig. 2 shows the spatial differences in the 1981–2020 means between the monthly-calculated NSWS and hourly-calculated NSWS. When calculating NSWS at the two different temporal resolutions, NSWS hourly-calculated is always greater than the monthly-calculated NSWS. Differences across the TP can reach 0.4 m s^{-1} in the higher-elevation regions, with an average difference of 0.2 m s^{-1} for the whole plateau in all three reanalyses. Differences may be related to the importance given at specific spatial- and time-scales in the two NSWS calculations. In the NSWS monthly-calculated, daily or sub-daily processes are not so relevant, as it only considers the aggregated statistics of the u and v wind components. This method may be more suitable for global studies, where large-scale atmospheric circulations are more relevant than local and short-time scale processes (Landberg 2016). When computing NSWS based on hourly u and v components, daily and/or sub-daily processes can be considered. Therefore, it is relevant to use hourly-calculated NSWS only for studies on

Fig. 2 Spatial differences between the annual means of monthly-calculated and hourly-calculated NSWS in ERAINT (**a**), ERA5 (**b**), and ERA5-Land (**c**) for 1981–2020
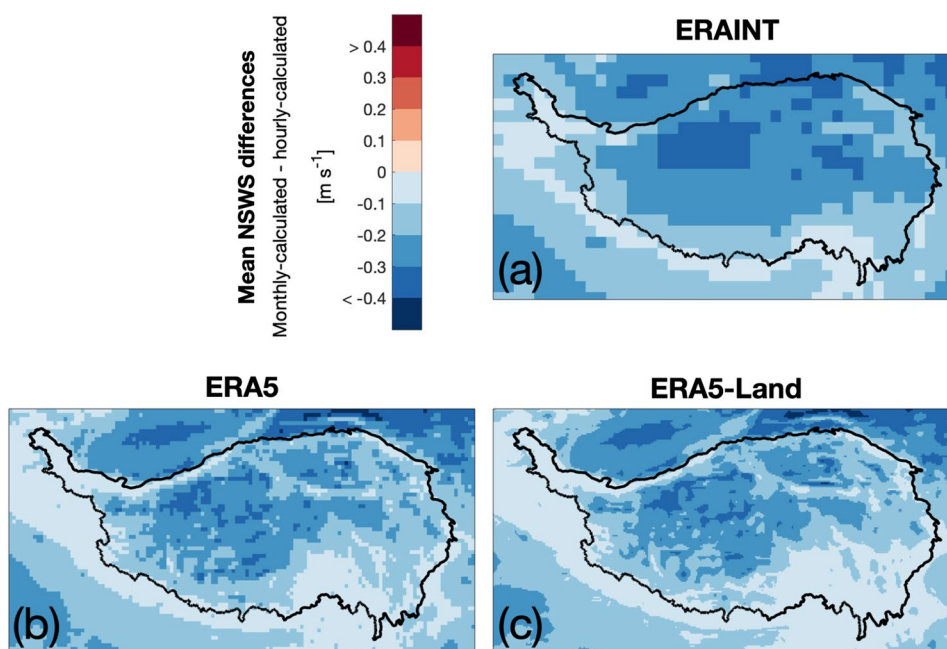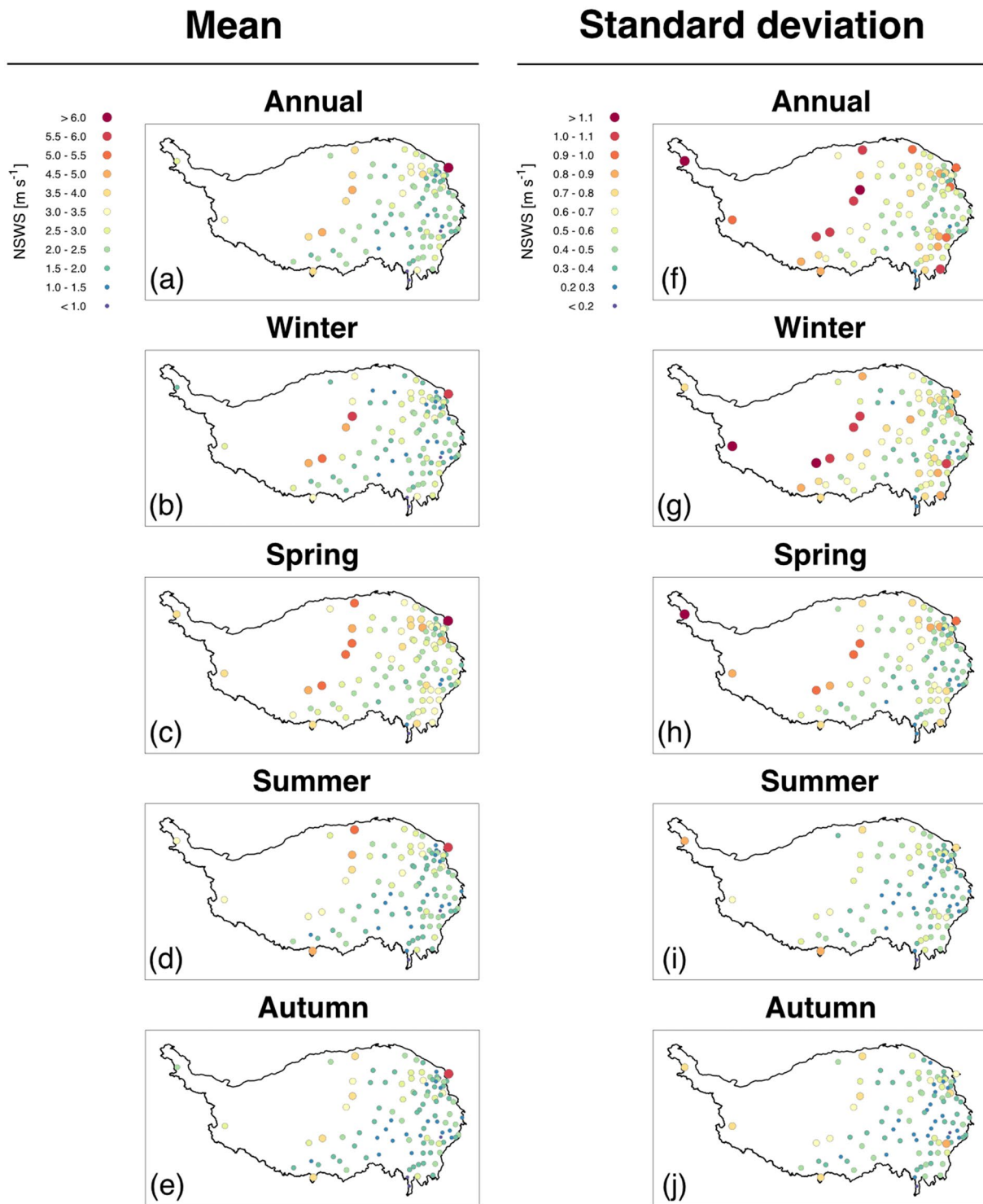
Fig. 3 Spatial distribution of the annual and seasonal means and the standard deviations of the observed NSWS for the 104 homogenized stations over the TP for 1960–2020

shorter-time or local scales. The TP is a region of extremely complex topography where local and short-time scale processes play a key role (Liu et al. 2009; Yang et al. 2004). Wind conditions are strongly affected by surface forcing as large-scale wind circulation is broken by localized circulations driven by valleys and mountains (Helbig et al. 2017; Rotach et al. 2015; Serafin et al. 2018). For this reason, we decide to use NSWS hourly-calculated in this study.
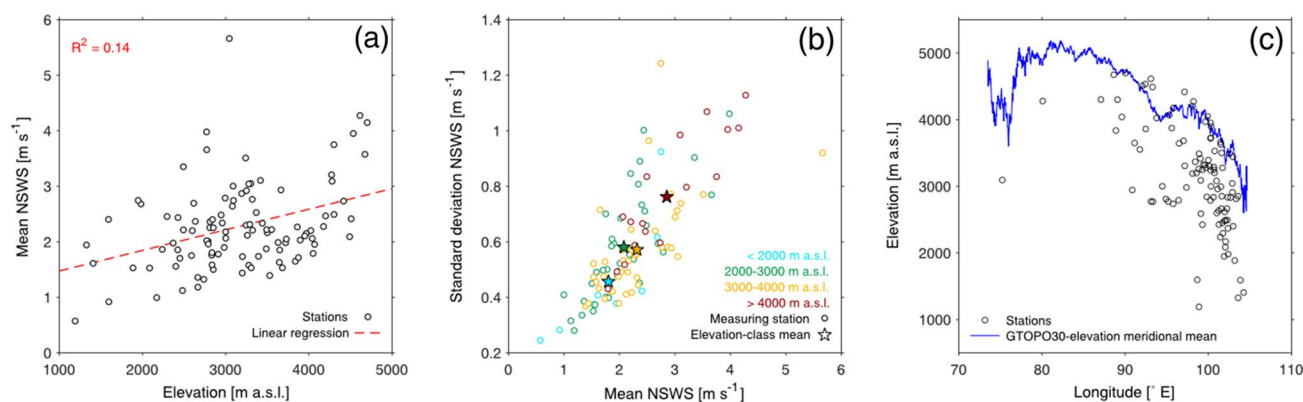
Fig. 4 Elevation dependency of NSWS: (**a**) Scatter plot of the 1960–2020 mean of NSWS for the 104 stations over the TP plotted against the station elevation. (**b**) Scatter plot of the 1960–2020 mean of NSWS for the 104 stations over the TP (circles) and for the 4 means of the elevation-classes (stars) plotted against the respective 1960– 2020 standard deviation. (**c**) Scatterplot of the elevation of the 104 stations over the TP plotted against the station longitude. The blue line is the elevation meridional-mean over the TP calculated using the GTOPO30 dataset

4 Results and discussion

4.1 Climatology of observed NSWS

Figure 3 shows the annual and seasonal spatial distribution of mean and standard deviation of observed NSWS for 1960–2020 over the TP. Annually, the few stations on the west and center of the plateau display greater mean NSWS (between ~3.5 and ~4.5 m s^{-1}) compared to the stations in the east and southeast (~2.0 m s^{-1}). The spatial pattern of the standard deviation of observed NSWS for 1960–2020 resembles the spatial pattern of the mean, with higher values (greater than ~1.0 m s^{-1}) for stations in the west and center of the plateau compared to stations in the east (Yao et al. 2018). Following this spatial distribution, it appears that stations with higher mean NSWS display also higher standard deviation, as shown by the scatter plot of mean versus standard deviation in Fig. S2 in the supplementary material. Seasonally, the spatial distribution with lower values of mean and standard deviation in the west does not change. Overall, there are greater values recorded for all the measuring stations during spring compared to winter, summer and autumn, and stations with greater mean are also the ones with greater standard deviation.

To identify the geographical features behind the detected spatial pattern, the mean NSWS of each station is plotted against the station elevation (Fig. 4a). It is evident that stations at higher elevations are the ones with greater mean NSWS. By grouping stations into classes with increasing averaged elevation, stations display greater mean and standard deviation of NSWS (e.g., red star vs. light-blue star; Fig. 4b). As stations in the west and center of the plateau are the ones located at higher elevation (Fig. 4c), the spatial pattern of Fig. 3 with stations on the west and center

of the plateau of greater NSWS mean and standard deviation is explained. Therefore, elevation differences driven by the topography are responsible for the spatial distribution of mean and standard deviation of observed NSWS, with station mean and standard deviation increasing for increasing elevation. Note that mean NSWS decreases from stations in the west to stations in the east when plotting the mean of NSWS of each station against the station longitude (Fig. S3 in the supplementary material). However, this zonal dependency of mean NSWS results from having just a few stations at high elevation in the west of the plateau. In fact, when using the GTOPO30 data to calculate the elevation meridional-mean and to see how elevation changes according to the longitude over the TP (Fig. 4c), it is shown that the plateau has greater altitude in the west compared to the east: the apparent zonal dependency is driven by the elevation dependency. The elevation dependency of NSWS (i.e., terrain enhances wind speed and high-elevation regions more influenced by strong large-scale synoptic flows) is not something new, and various studies (McVicar et al. 2007; Miller and Davenport 1998; Wood 2000) have already shown that wind speed increases exponentially with increasing altitude, especially over the TP (Yao et al. 2018).

To further explore the climatology of NSWS over the TP, the seasonal cycle for 1960–2020 is analyzed. As shown by Fig. S4 in the supplementary material, greater NSWS is recorded during spring compared to the rest of the seasons, in line with what has been shown by Li et al. (2017), Li et al. (2021a, b), and Zhao et al. (2019). The wind is stronger during spring because it is the time of the year when extra-tropical cyclones are active (Li et al. 2021a, b). By using k-means clustering, differences in the seasonal cycle anomalies among the observed NSWS series are explored. We identify three classes of stations with different
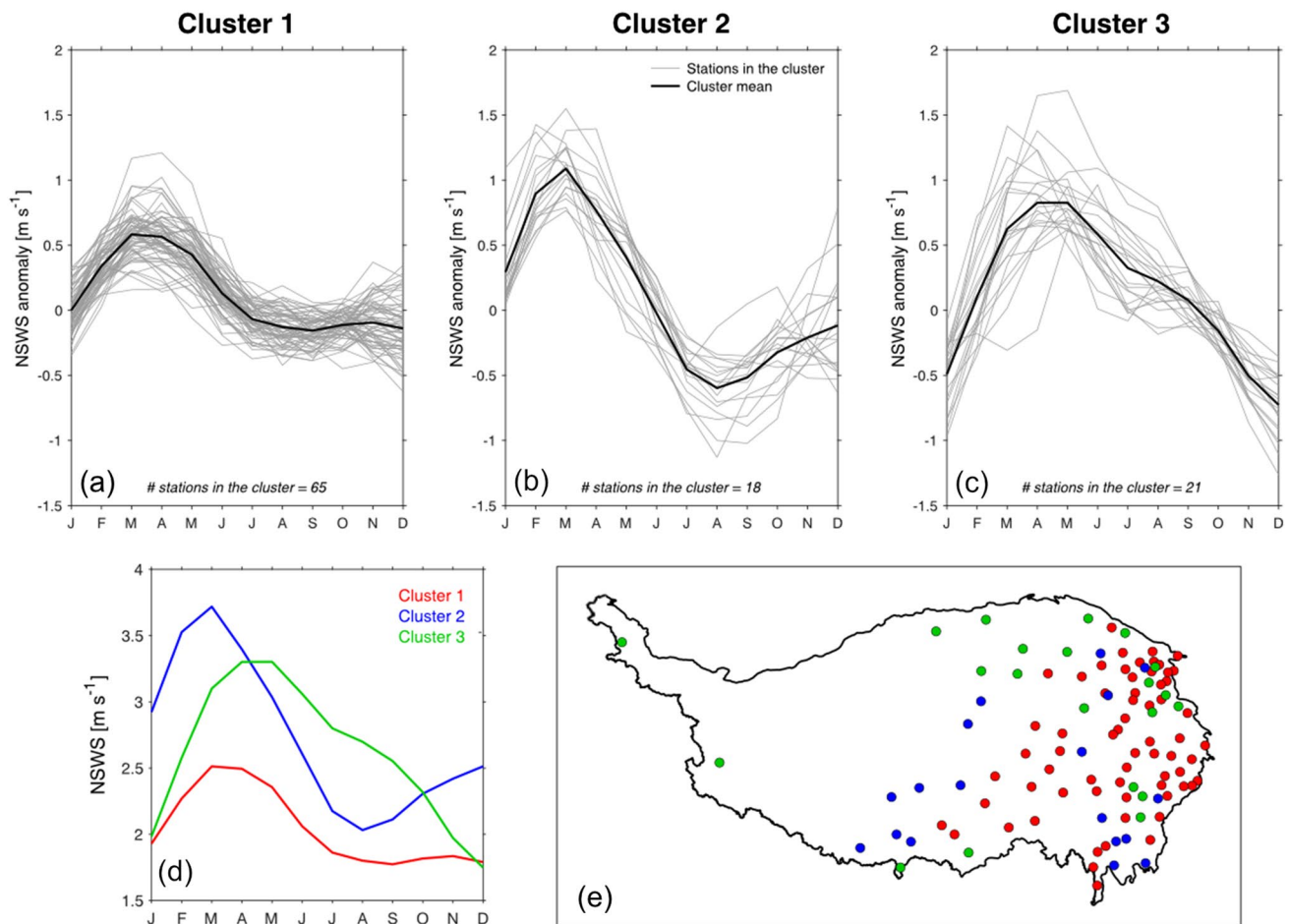
Fig. 5 Seasonal cycle clusters: (**a-c**) Clustering of the mean seasonal cycle of NSWS anomalies for the 104 stations over the TP for 1960–2020. Grey lines represent the seasonal cycles of each station series in the given cluster, while the seasonal cycle cluster-mean (i.e., average over all the stations in the given cluster) is plotted as the black line. (**d**) Cluster-averaged (i.e., averaged over all the stations in the cluster) seasonal cycles of NSWS over the TP for 1960–2020. (**e**) Spatial distribution of the seasonal cycle clusters of the 104 stations over the TP. Stations in *Cluster 1* are shown as red dots, stations in *Cluster 2* as blue dots, and stations in *Cluster 3* as green dots

seasonality (Fig. 5). Note that we chose three partitions in the cluster analysis because with this number it is reached a good balance between coherent patterns and sufficient distinction between classes. One class (hereafter, *Cluster 1*, which includes most of the stations – 65 stations; Fig. 5a) displays a NSWS maximum during spring (i.e., March and April). Another class (*Cluster 2*; Fig. 5b) includes 18 NSWS series that have a maximum in February-March-April and a minimum in July-August-September. The third class (*Cluster 3*; Fig. 5c) includes 21 stations with greater NSWS during spring and early-summer (i.e., from March to July) compared to the rest of the year. Looking at the magnitude differences in the NSWS seasonal cycle between the three classes (i.e., when plotting the mean NSWS annual cycle for each cluster identified using the seasonal cycle NSWS anomalies; Fig. 5d), the mean *Cluster 2* seasonal cycle is overall greater (~ 2.0–3.8 m s^{-1}) than the one for *Cluster*

1 (~ 1.8–2.5 m s^{-1}). Similar to the highest NSWS values recorded in *Cluster 2*, *Cluster 3* stations reach on average ~ 1.8–2.5 m s^{-1} during late spring. Figure 5e shows the spatial distribution of the seasonal cycle clusters. Stations belonging to *Cluster 1* are mostly located in the east of the TP, while stations from *Cluster 2* are found in the center of the plateau, with only a few stations in the east (mostly southeast). *Cluster 3* stations are located all along the western and southern border of the TP, in the north, and a few are also found in the east. Unfortunately, the sparse and biased distribution of measuring stations over the TP is a challenge for the comprehensive understanding of the spatial pattern of NSWS clusters across the plateau. For example, does *Cluster 2* include all stations at the higher elevations of the center of the plateau? For answering to such types of questions, it is necessary to analyze a more spatially complete dataset, such as the reanalysis outputs (see Sect. 4.2).
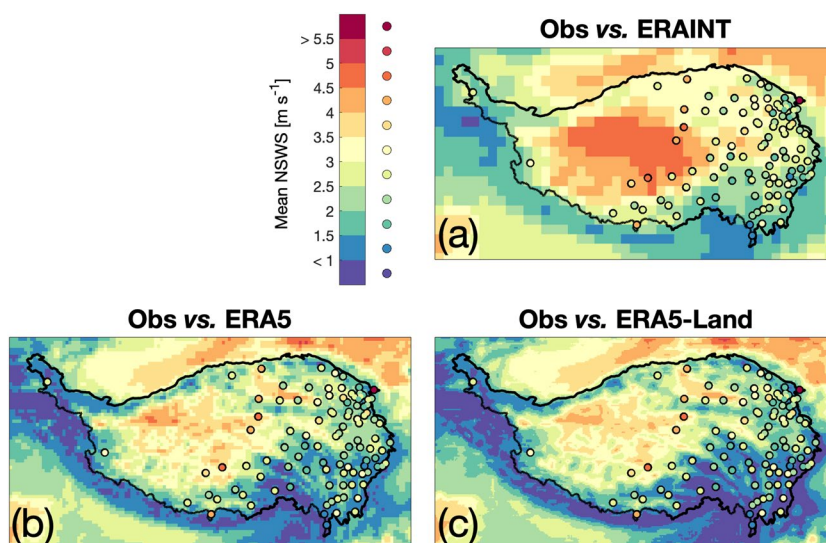
Fig. 6 Spatial distribution of the annual-mean NSWS calculated for 1981–2018 using observations (colored dots) and ERAINT (**a**), ERA5 (**b**), and ERA5-Land (**c**)
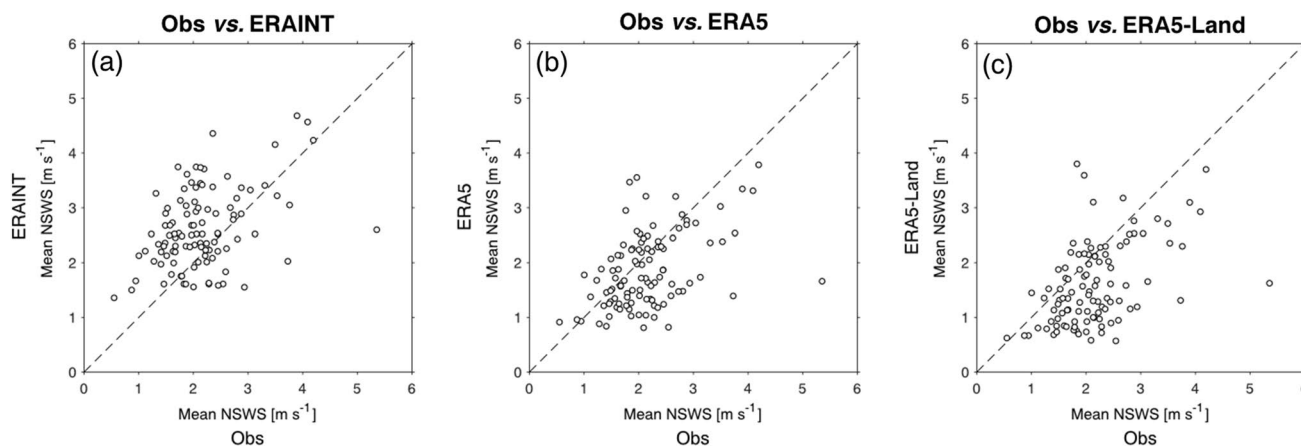

Fig. 7 Scatter plot of the 1981–2018 annual-mean of the observed NSWS of the 104 stations over the TP plotted against the respective NSWS mean of the ERAINT closest grid points (**a**), of the ERA5 closest grid points (**b**), and of the ERA5-Land closest grid points (**c**)

4.2 Comparison between observations and reanalyses

To investigate the performance of the selected ECMWF reanalyses in simulating NSWS, the spatial distribution of mean NSWS for 1981–2018 is plotted in Fig. 6 for observations, ERAINT, ERA5, and ERA5-Land. Despite the differences in the horizontal resolution, all three datasets are able to capture the higher NSWS in the center of the plateau. But, thanks to the higher resolution, better model physics, more data assimilated, and its more advanced assimilation method, ERA5 and ERA5-Land show improvements in simulating mean NSWS due to more-local topographic features, which ERAINT cannot reproduce. For example, especially in the southeast of the TP, the latest reanalyses

can differentiate between NSWS conditions in valleys (lower values) and along ridges (higher values). In general, ERAINT tends to overestimate mean NSWS over the TP (Fig. 7). Even if both ERA5 and ERA5-Land slightly underestimate the NSWS conditions, they better match the spatial differences in mean NSWS over the plateau compared to ERAINT. Statistics shown in Fig. 8 enable a more detailed comparison between the performance of the three reanalysis datasets in simulating NSWS during 1981–2018. Mean Pearson's correlation does not differ notably among the reanalyses (between 0.4 and 0.5), even when the seasonal cycle is removed from the monthly NSWS series (mean correlation drops almost equally by ~0.12 for all three datasets). Mean RMSE is greater for ERAINT and ERA5-Land (0.96 and 0.89 m s^{-1}, respectively) compared to ERA5 (0.8 m s^{-1}).
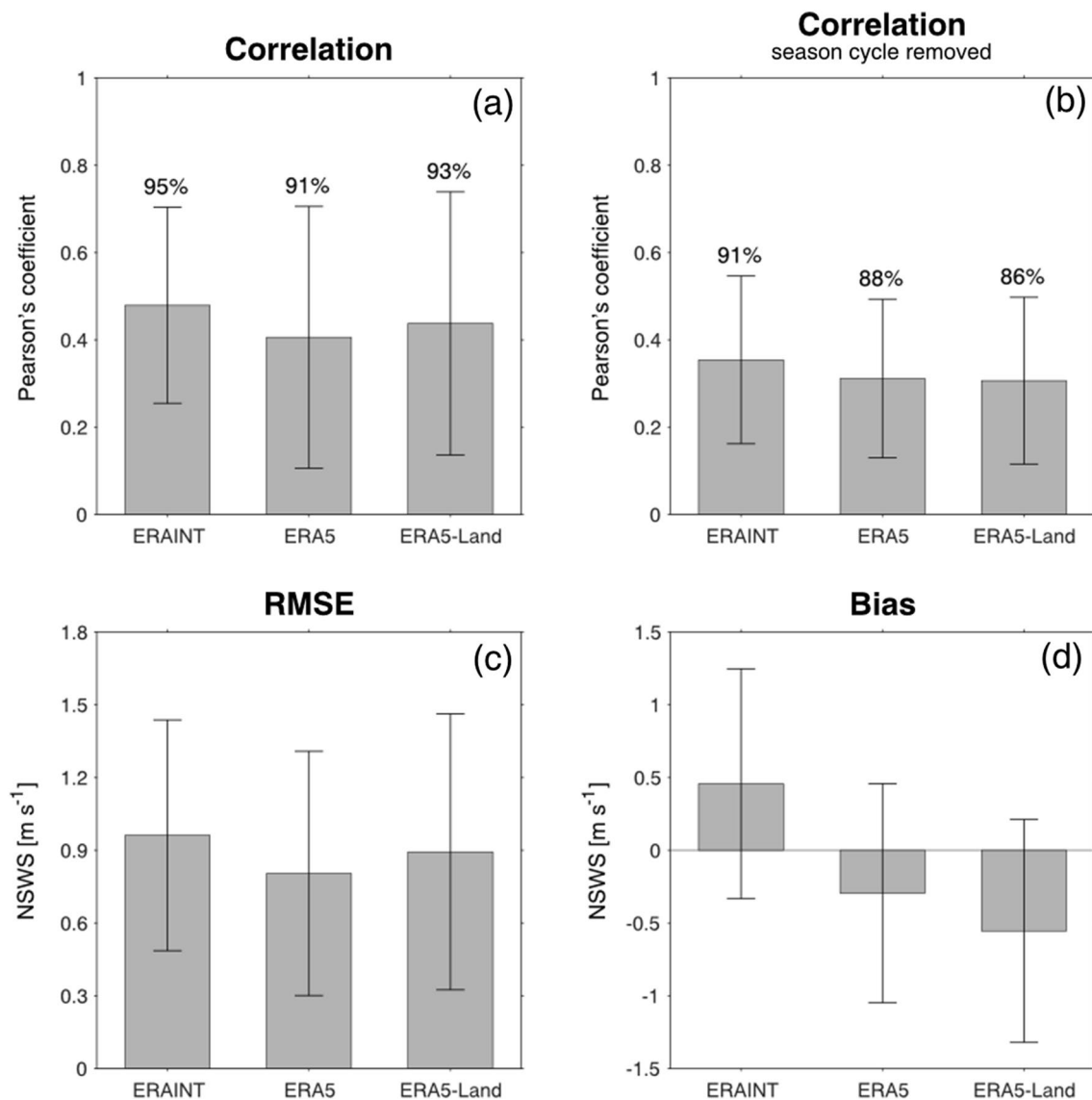
Fig. 8 Averaged (i.e., averaged over all the stations/closest grid points) statistics of comparison (i.e., (**a**) Pearson's correlation, (**b**) Pearson's correlation without seasonal cycle, (**c**) RMSE, and (**d**) bias (modeled minus observed) between monthly-averaged observed NSWS series and monthly-averaged reanalyzed NSWS series from ERAINT, ERA5, and ERA5-Land for 1981–2018. For the Pearson's correlation, it is also reported the percentage of the closest grid points showing significant correlation at significant level $p < 0.05$. The error bar (± 1 standard deviation around the mean value) shows the standard deviation of the statistic metric calculated for all the stations/closest grid points

The large biases in ERAINT and ERA5-Land, which is positive for the former (0.5 m s^{-1}) and negative for the latter dataset (0.6 m s^{-1}), account substantially to such large RMSEs. As already seen from Fig. 7, similar to ERA5-Land, ERA5 tends to underestimate NSWS, with a mean bias of 0.3 m s^{-1}. Overall, the performance of the three reanalyses in simulating monthly NSWS series for 1981–2018 does not differ significantly in terms of mean correlation, mean RMSE, and mean bias. Only ERA5 displays a smaller mean RMSE and bias compared to both ERAINT and ERA5-Land, even if it is also negatively biased.

The improvements in NSWS simulation of ERA5 and ERA5-Land can be detected when looking at the mean seasonal cycle. Consistent with the results of Fig. 7, mean NSWS seasonal cycle of ERA5 and ERA5-Land is negatively biased but captures the higher NSWS conditions observed during March and April (Fig. S4 in the supplementary material). In addition, when applying the k-mean clustering to modeled NSWS anomaly series, only the seasonal cycles of ERA5 and ERA5-Land grid-series can be clustered in three classes (Fig. 9). Within the ERAINT data, just two classes with different seasonality can be identified. Figure 10
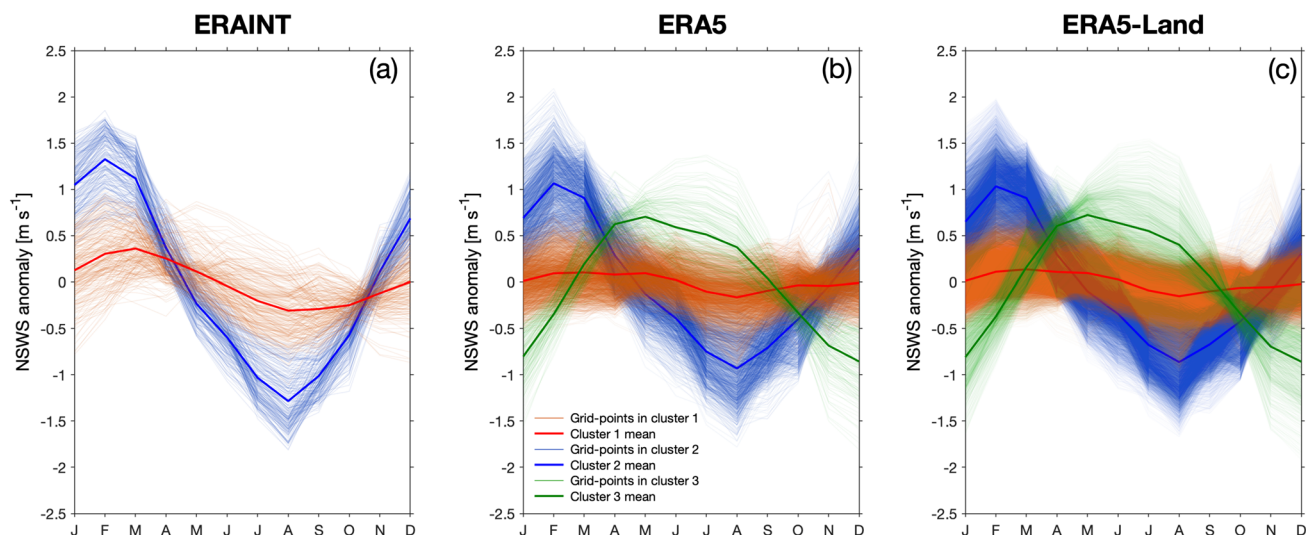
Fig. 9 Clustering of the 1981–2018 mean seasonal cycle of NSWS anomalies for the 104 closest-grid series of ERAINT (**a**), ERA5 (**b**), and ERA5-Land (**c**). Light-colored lines represent the seasonal cycles of each closest grid point series in the given cluster, while the seasonal cycle cluster-mean (i.e., average over all the closest grid point series in the given cluster) is plotted with the dark-colored thicker line
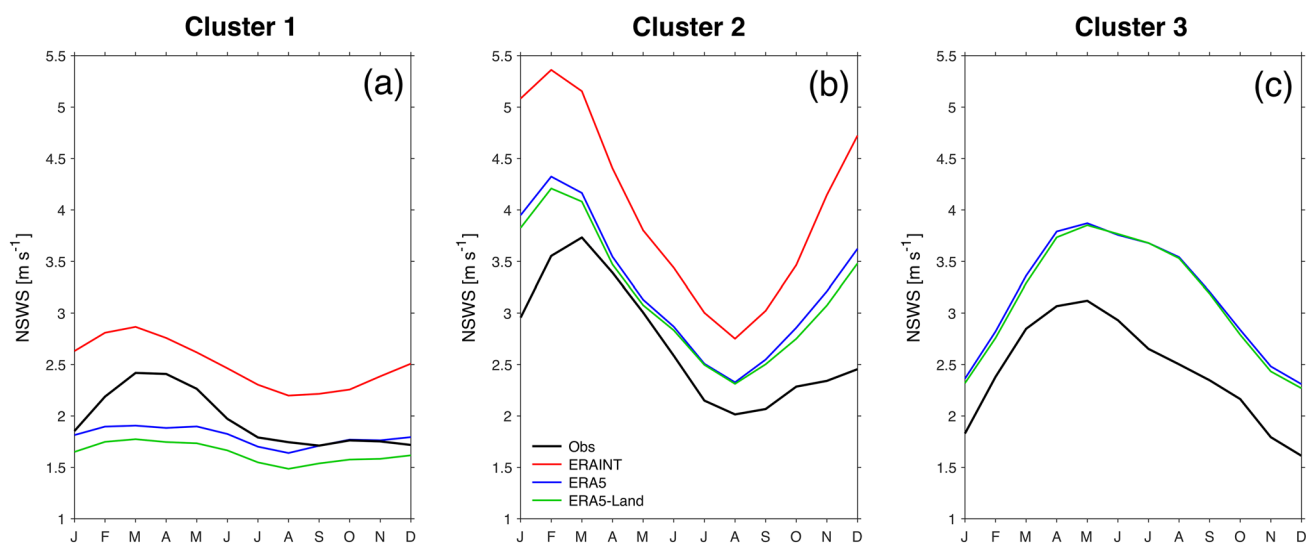

Fig. 10 Comparison of cluster-averaged (i.e., averaged over all the stations/closest grid points in the cluster) series of the 1981–2018 mean seasonal cycles of NSWS calculated using observations (black line), ERAINT (red lines), ERA5 (blue line), and ERA5-Land (green line)

compares the cluster-averaged (i.e., averaged over all the stations/closest grid points in the cluster) seasonal cycles of NSWS calculated using observations with the ones calculated using ERAINT, ERA5, and ERA5-Land. Here we can see that ERAINT captures the annual variations in the two classes that it simulates, even if it overestimates the annual mean of NSWS. In contrast, both ERA5 and ERAINT are negatively biased when simulating the NSWS seasonal cycle of *Cluster 1* and partly lack in capturing the greater wind magnitudes during March-April. But, in *Cluster 2* and *Cluster 3*, the two latest ECMWF reanalyses, even if positively

biased (bias smaller than the one shown by ERAINT), properly follow the observed annual variations of NSWS.

The spatially-complete reanalyses can now be used to explore how the different classes are distributed over the TP (Fig. 11), something we could not do using the observational dataset of sparse and biased-distributed in-situ measuring stations (see Sect. 4.1). *Cluster 1* (red areas) in all three datasets surrounds the plateau and it largely occupies the eastern side of the plateau. Instead, *Cluster 2* (blue areas) is dominant in the center-west of the TP and over a few limited areas in the east. *Cluster 3*, which appears in ERA5
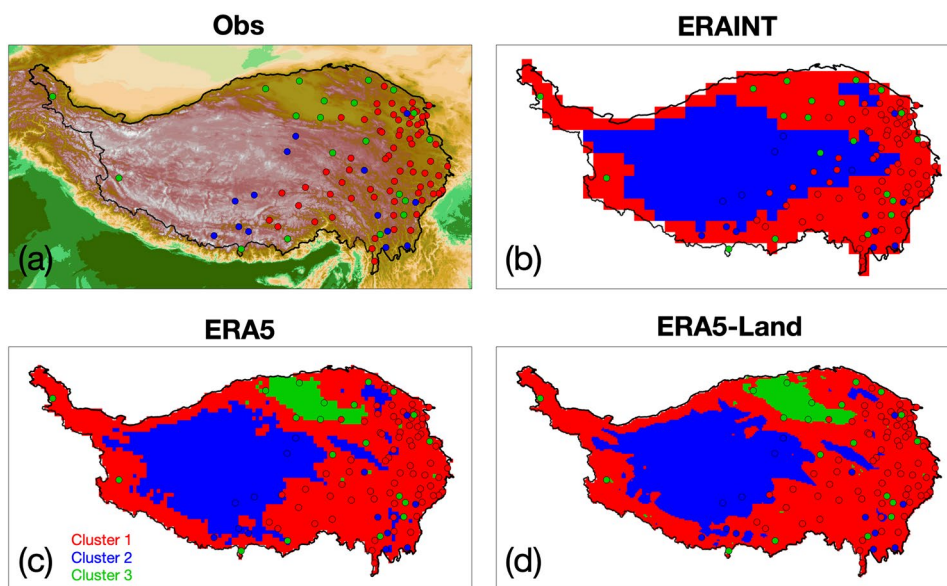
Fig. 11 Spatial distribution of the NSWS seasonal-cycle clusters calculated for 1981–2018 using observations (**a**), ERAINT (**b**), ERA5 (**c**), and ERA5-Land (**d**)
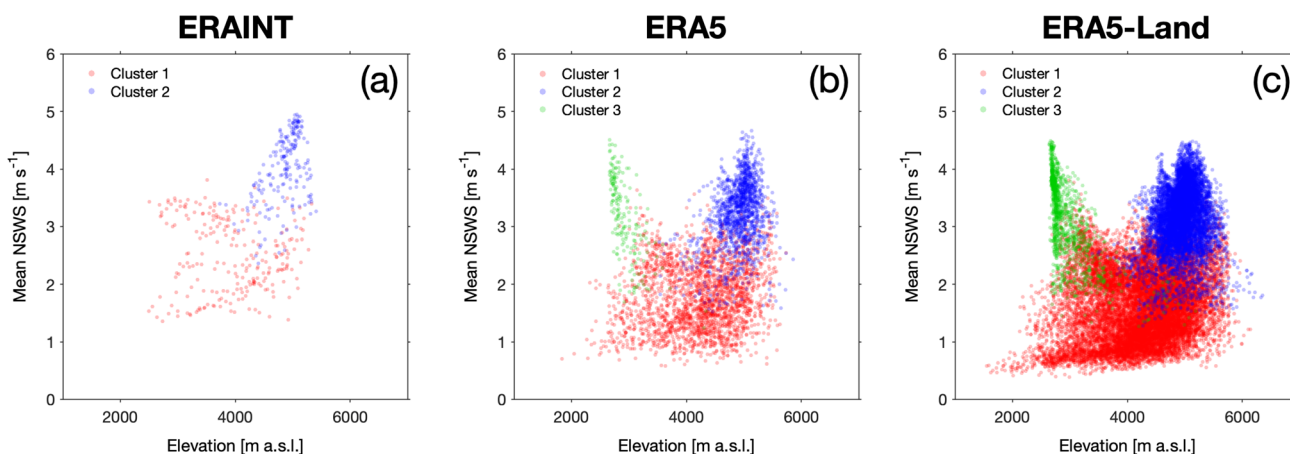

Fig. 12 Scatter plot of the modeled elevation of the grid points over the TP plotted against their NSWS mean for 1981–2018 in ERAINT (**a**), ERA5 (**b**), and ERA5-Land (**c**). Each scatter-point is colored according to the class it belongs to: *Cluster 1* in red, *Cluster 2* in blue, and *Cluster 3* in green

and ERA5-Land, occupies a large area in the northeastern plateau, which corresponds to the Qaidam basin, the largest topographic depression inside the TP (Yin et al. 2008). Figure 12 plots the 1981–2018 mean NSWS of each grid point in a given dataset with its modeled elevation, with the scatter points colored according to the class they belong to. In all the reanalyses, grid points from *Cluster 1* go from the highest to the lowest elevations, while grid points in *Cluster 2* are the ones with the higher elevations and the greatest mean NSWS. *Cluster 3*, which appears only in ERA5 and ERA5-Land, includes grid points in a shallow band with elevation between 2,800–3,500 m a.s.l. (i.e., the depression of the Qaidam basin) with mean NSWS between 2 and

4.5 m s^{-1} (generally higher than the one of *Cluster 1* and in the same range of *Cluster 2*). The clear differences in the seasonal cycle at the Qaidam basin can be associated with the blocking effect of the surrounding mountainous terrain (Zhao et al. 2019). In fact, as the Qaidam Basin is aligned north-west, it shows greater wind conditions during summer when the dominant southwesterly winds prevail strengthened by the blocking effect of the surrounding terrain.

Not only measuring stations located in the Qaidam basin are classified in *Cluster 3*, but various other stations over the TP are grouped in *Cluster 3* (Fig. 12). Similarly, a few grid points of ERA5 and ERA5-Land outside the Qaidam basin appear to belong to *Cluster 3*. The reason behind such

localized *Cluster 3* stations and grid points could be related to the valley and mountain orientations: for example, the main wind direction coincides with the path of the westerly jet stream and the orientation of valleys and mountains (Yao et al. 2018). In ERA5 and ERA5-Land, where complex topography can only be modeled partly, *Cluster 3* grid points outside the Qaidam basin are uncommon.

The reason why ERAINT only identifies two classes when clustering the seasonality, while the latest datasets can see three classes (i.e., the Qaidam basin's wind conditions), may be related to the lower resolution, the worse modeled physics, less data assimilated, and the less advanced assimilation method compared to ERA5 and ERA5-Land (Dee et al. 2011). For example, thanks to the higher resolution, the orography is better simulated in ERA5 and ERA5-Land: the mean elevation difference between actual station elevations and modeled elevations of the closest grid point of ERAINT is −645.3 m, and it decreases for ERA5 and ERA5-Land (−599.7 m and −450.2 m, respectively). The more realistic topographic representation may help to better identify the different NSWS conditions in the comparatively low-elevated area of the Qaidam basin. Of course, the higher spatial resolution cannot explain alone the better performance of ERA5 and ERA5-Land compared to ERAINT: it is important to consider it all together with the improvements in model processes, core dynamics, and data assimilation. This is supported by the similar performance of ERA5-Land and ERA5 in simulating NSWS statistics. In fact, even if ERA5-Land has a finer horizontal spacing, it does not show any significant improvements compared to ERA5, as it can be considered as a re-run of ERA5. It results indeed from forcing the land surface component with

low atmospheric meteorological fields from ERA5, with no additional atmospheric/oceanic coupling or data assimilation scheme (Gomis-Cebolla et al. 2023).

To summarize, ERA5 better simulates NSWS over the TP compared to ERAINT probably due to its considerable increase in horizontal and vertical resolution, as well as temporal resolution, and a decade of improvements in the representation of model processes and data assimilation (Hersbach et al. 2018). The simulated NSWS in ERA5-Land do not match better the observed one compared to ERA5, as ERA5-Land shares with ERA5 most of the parametrizations and does not benefit from any changes in the physics of the model or from the data assimilation (Muñoz-Sabater et al. 2021). To notice that the elevation of the measuring stations is generally lower than the one of the nearest grid cells, especially in the mountainous southern TP (Li et al. 2017). This is because most of the stations across the plateau are located in valleys, where they are easier to access. Therefore, the station elevation may not be a representation of the closest grid-point, and such elevation mismatch could contribute to the differences between observed and simulated wind. This issue is related to the fundamental mismatch between the spatial representativeness of in-situ observations, which are necessary collected at precise locations, and that of gridded climate model outputs, which instead represent mean values over an area (Avila et al. 2015). Therefore, it is important to underline that discrepancies between observations and model outputs can also be partly attributed to the problematic comparison of point observations to values on a latitude-longitude grid, as observed NSWS is highly dependent on the precise location of the station within the terrain complexity, while model output only represents the grid mean value.

Fig. 13 Spatial distribution of the 1991–2018 mean of NSWS calculated using ERA5 (**a**), WRF-9km (**b**), and HAR (**c**)
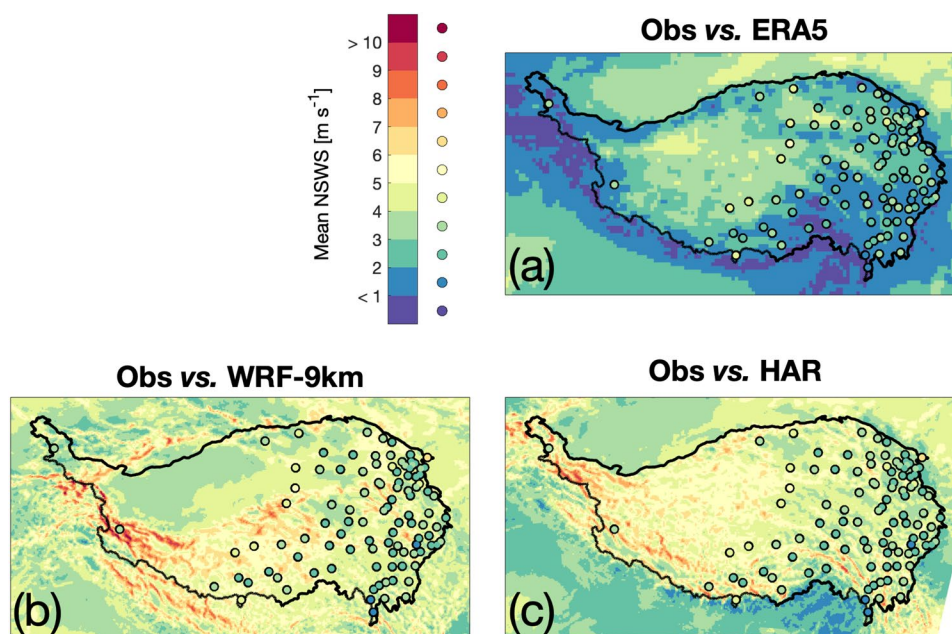
4.3 The added value of downscaling

To evaluate if the downscaling adds value to the NSWS simulations compared to the downscaled product, the spatial distribution of mean NSWS for 1991–2018 is plotted in Fig. 13 for observations, ERA5 (i.e., the reanalysis which has shown to better simulate NSWS over the TP), and the two downscaled products WRF-9km and HAR. As already seen from Fig. 6, ERA5 shows higher NSWS values in the center of the plateau (as also seen in the observations) and simulates NSWS conditions following the complex terrain features (e.g., the large valleys in the southeast of the TP). Instead, WRF-9km only shows strong mean winds in the southern part of the plateau, with weaker winds from the center to the north. Mean NSWS in HAR is greater in the west, and it decreases by moving to the east. HAR, similar to WRF-9km, does not display the feature with higher wind conditions in the center-west of the TP, and a generally lower NSWS in all its surroundings. Fig. S5 in the supplementary material confirms those discrepancies between observed NSWS and NSWS from the two downscaled products. When plotting the mean observed NSWS against the simulated one, WRF-9km poorly simulates wind conditions: all the scatter-points are greatly positively biased (i.e., NSWS higher in WRF-9km compared to observations). For HAR, biases in the modeling are also seen as modeled NSWS means are in general higher than the observed ones. When it comes to the modeling of the seasonal cycle (Fig. S6 in the supplementary material), in a similar way both WRF-9km and HAR overestimate the observed one, not showing any improvements compared to the downscaled ERA5. For these reasons, when it comes to aggregated climatology, the two downscaled products WRF-9km and HAR do not better simulate NSWS over the TP compared to ERA5. But the added value of downscaled products should be searched in the better modeling of shorter spatial- and time-scale processes, as the diurnal cycle (Ou et al. 2020).

Therefore, we explore here the mean diurnal cycle of observed NSWS and then we compare it with the one simulated by ERA5 and the two downscaling products (Fig. 14). Figure 14a shows that the mean 3-hourly sub-daily variations of NSWS calculated using the 27 stations of the Had-ISD dataset peaks at 9 UTC (~ 15–16 local time), in line with what shown by Zhao et al. (2019). The annual averaged diurnal cycle from ERA5 and WRF-9km also peaks around 9 UTC. Instead, the diurnal cycle of HAR peaks earlier (around 6 UTC). WRF-9km displays the lowest correlation value compared to ERA5 and HAR. In addition, WRF-9km largely overestimates the magnitude of the diurnal variations (mean positive bias and RMSE of ~ 2.5 m s^{-1}). While HAR exhibits a large mean RMSE of approximately 1.5 m s^{-1}, it is important to note that the high positive bias (~ 1.3 m s^{-1}) is a substantial component of this error. In contrast, ERA5

demonstrates a considerably smaller mean RMSE compared to both WRF-9km and HAR, with an average negative bias of approximately 0.5 m s^{-1}.

To further explore the observed 3-hourly diurnal cycle of NSWS, we apply the k-mean clustering to the dataset of 27 observed series. By conducting the cluster analysis with an increasing number of classes (Fig. 15 top row), the anomalies of the mean diurnal cycle do not drastically change in shape (always peak at 9UTC), but the peak becomes more pronounced. The more pronounced diurnal cycle seems to be partly related to station elevation: the classes which peaks more, are the ones with greater mean elevation. When looking at the clusters identified in the simulated diurnal cycles (Fig. 15 bottom row), all the classes in ERA5 peaks at 9 UTC and differ only in how this peak is pronounced. This is partly shown also in HAR, but, especially in WRF-9km, the identified classes do not only differ in how the 9 UTC peak is pronounced, but also in the time when it is recorded and in the overall shape of the mean diurnal variations.

Zhao et al. (2019) previously investigated diurnal variations in NSWS over the TP, finding remarkable regional characteristics with respect to the diurnal variations. For example, in the eastern of the plateau, the minimum and the maximum recorded wind speed occur about 1 h later than in the west; or the diurnal cycle at the stations in the Qaidam Basin differ significantly from the one observed at the other stations elsewhere on the plateau. Unfortunately, for this study hourly data were not available, and the use of 3-hourly outputs for exploring the diurnal cycle characteristics may mask possible regional differences.

Therefore, from what is shown here, HAR and WRF-9km do not improve the simulation of the mean diurnal cycle over the TP, even if additional analysis (using hourly statistics) may be needed. To conclude, both HAR and WRF-9km do not show a significant added value in the simulation of NSWS statistics over the TP compared to the downscaled product ERA5. The two dynamical downscalings may improve their performance in simulating NSWS over the TP by better considering the orographic impact on surface flow once the effects of subgrid-scale topography (i.e., topographic drag) are included through correct parametrization (Jiménez and Dudhia 2012). Zhou et al. (2017) and Zhou et al. (2018) highlight that the subgrid orographic drag scheme, especially the turbulent orographic form drag scheme, can efficiently reduce NSWS biases in WRF simulations over the TP, a region surrounded by high mountains with high orographic variance, where the local climate is very sensitive to orographic drag. Therefore, an insufficient representation of subgrid orography can lead to systematic biases in numerical simulations over complex terrains, and improvements in the modeling of atmospheric circulation are reached only when the effects of subgrid orographic drag are properly parameterized. Moreover, it is necessary
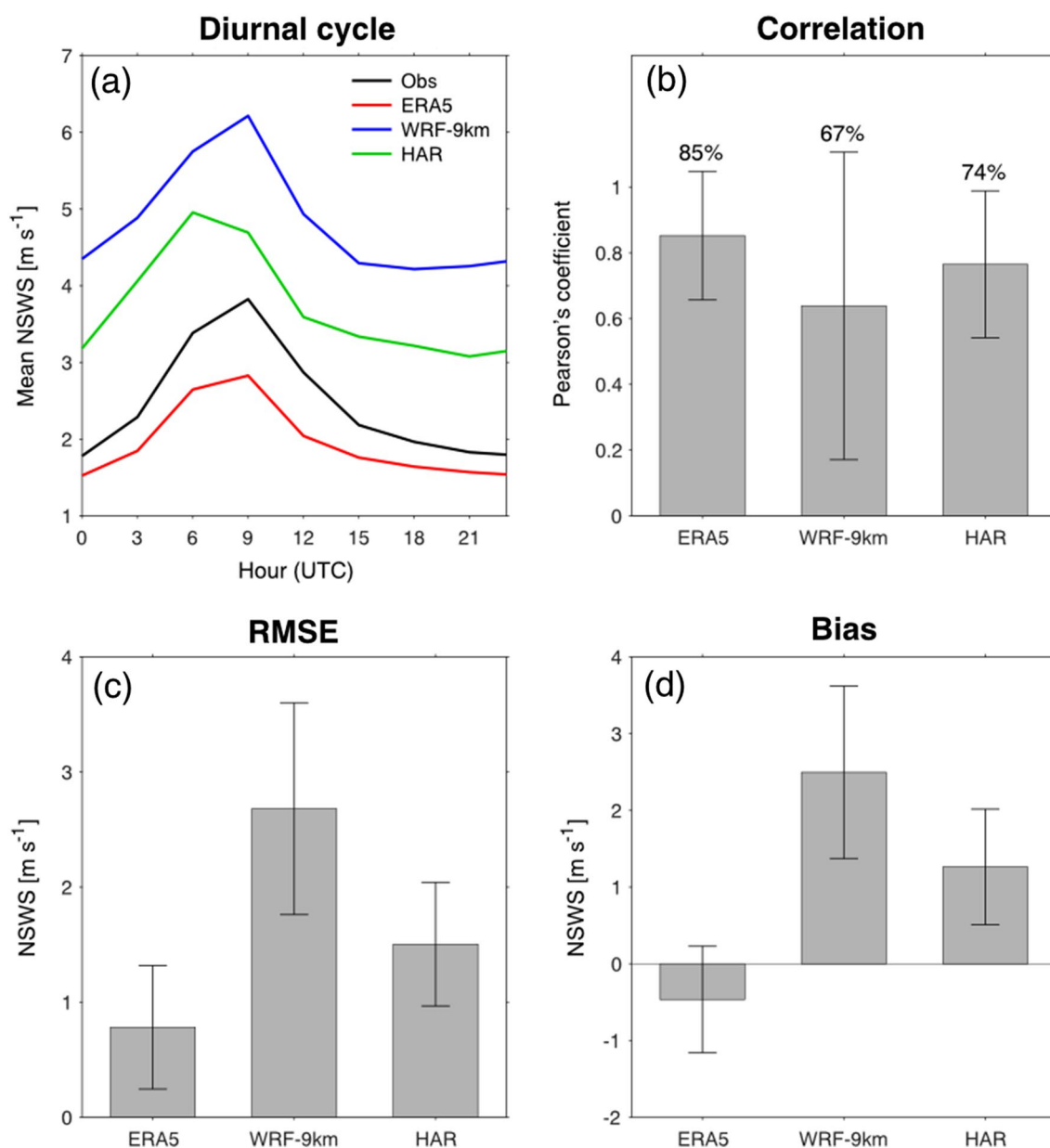
Fig. 14 Comparison between observed and simulated NSWS diurnal cycle. (**a**) Mean 3-hourly diurnal cycle of NSWS calculated using observations (black line), ERA5 (red line), WRF-9km (blue line), and HAR (green line) for 2017–2018. (**b**) Averaged (i.e., average over all the stations/closest grid points) Pearson's correlation between mean 3-hourly diurnal cycle from observed NSWS and from ERA5, WRF-9km and HAR for 2017–2018. It is reported the percentage of the closest grid points showing significant correlation at significant level $p < 0.05$. (**c**) Averaged (i.e., averaged over all the stations/closest grid

points) RMSE between mean 3-hourly diurnal cycle from observed NSWS and from ERA5, WRF-9km and HAR for 2017–2018. (**d**) Averaged (i.e., averaged over all the stations/closest grid points) bias (modeled minus observed) between mean 3-hourly diurnal cycle from observed NSWS and from ERA5, WRF-9km and HAR for 2017–2018. The error bar (±1 standard deviation around the mean value) shows the standard deviation of the statistic metric calculated for all the stations/closest grid points

to consider the identified errors within ERA5 when explaining the poor performance of the two downscaling products. Since ERA5 serves as the common data source for both WRF-9km and HAR, providing the lateral boundary

conditions, any systematic biases inherent in the reanalysis dataset can propagate into the regional climate model simulation through the model input boundaries (Kim et al. 2023).
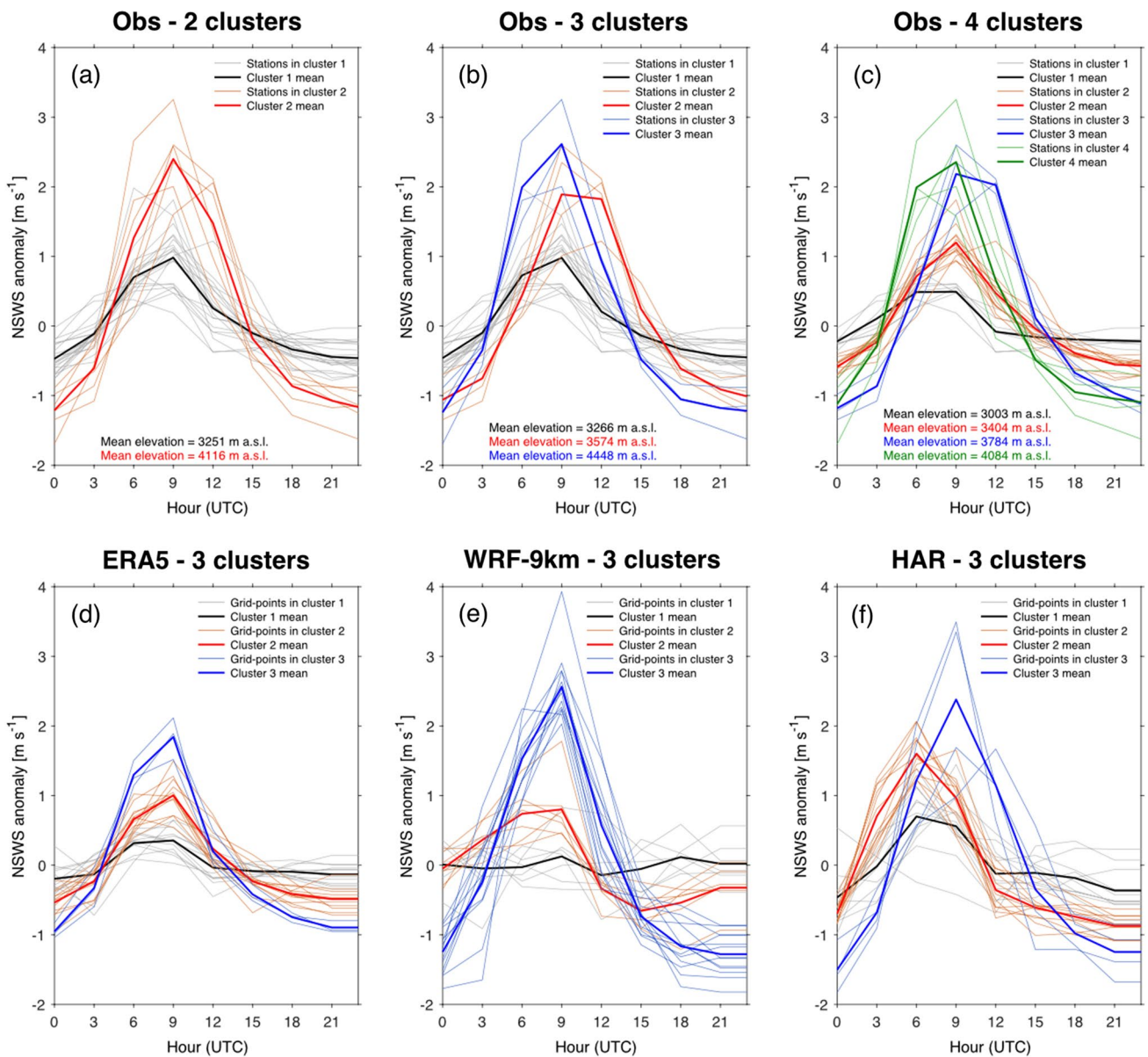
Fig. 15 Clustering of the mean 3-hourly diurnal cycle of observed and simulated NSWS anomalies for 2017–2018. In particular, on the top row: Clustering of the mean 3-hourly diurnal cycle of observed NSWS anomalies for 2017–2018 using 2 clusters (**a**), 3 clusters (**b**), and 4 clusters (**c**). On the bottom row: Clustering (with 3 classes) of the 2017–2018 mean 3-hourly diurnal cycle of NSWS anomalies from the closest grid points of ERA5 (**d**), WRF-9km (**e**), and HAR (**f**). Light-colored lines represent the diurnal cycles of each station/ closest grid point series in the given cluster, while the diurnal cycle cluster-mean (i.e., average over all the stations/grid points in the given cluster) is plotted with the dark-colored thicker line

5 Summary and conclusions

This study explored the climatology of NSWS over the TP using observations, reanalysis products, and high-resolution climate model simulations. The analysis of observed data revealed that the mean and standard deviation of NSWS is greater at the stations located in the central areas of the plateau, proving evidence that wind speed increases with increasing altitude over the TP. In addition, based on wind characteristics such as mean values and seasonal cycles, three distinct regions with different wind regimes were identified: (1) the central areas of the plateau, characterized by higher average elevation than the rest of the TP; (2) the eastern and the peripheral regions of the TP; and (3)

the topographic depression of the Qaidam basin, where the blocking effect of the surrounding mountainous terrain plays a significant role.

ERA5 is the reanalysis dataset which matches better the measured NSWS. Compared to its predecessor ERAINT, which can only represent two regions of different wind conditions, ERA5 is able to represent the three identified wind regimes: this improvement should be likely attributed to its finer spatial and temporal resolution, better model physics, more data assimilated, and the more advanced assimilation method. However, the newest ERA5-Land does not demonstrate advances compared to ERA5, as it primarily replays the land component of ERA5 with a finer spatial resolution, without any improvements in the parametrization scheme and model physics.

To assess the added values of dynamical downscaling, two different downscaling products of ERA5 (i.e., WRF-9km and HAR) were compared against the observations. However, both dynamical downscaling products fail to capture the observed spatial distribution characteristics of NSWS and do not improve the simulation of the 3-hourly diurnal cycle compared to ERA5. Therefore, it can be concluded that these high-resolution regional models do not add value in reproducing the observed NSWS climatology compared to ERA5. Consequently, the outputs of these regional models should not be prioritized over those of ERA5 when simulating NSWS statistics over the TP.

The biases of NSWS in the dynamical downscalings may partly result from an insufficient representation of subgrid orography through parametrization. Therefore, the ability of dynamical downscaling to simulate NSWS may be enhanced by including the topographic drag through appropriate parametrization of subgrid orographic drag. This aspect should be explored by analyzing the year-long WRF simulation which includes the turbulent orographic drag scheme implemented by Zhou et al. (2018). This analysis will be conducted within the framework of the Convection-Permitting Third Pole (CPTP) project, a Flagship Pilot Study (FPS) endorsed by the World Climate Research Programme-Coordinated Regional Climate Downscaling Experiment (WCRP-CORDEX) (http://rcg.gvc.gu.se/cordex_fps_cptp/; last accessed 7 August 2023).

Declarations

References

Aguilar E, Auer I, Brunet M, Peterson TC, Wieringa J (2003) Guidelines on climate metadata and homogenization. WMO Technical Document No. 1186. https://library.wmo.int/doc_num.php?explnum_id=10751 Accessed 7 Aug 2023

American Meteorological Society (AMS) (2013) Regional climate model. Glossary of Meteorology. https://glossary.ametsoc.org/wiki/Regional_climate_model Accessed 7 Aug 2023

Avila FB, Dong S, Menang KP, Rajczak J, Renom M, Donat MG, Alexander L (2015) Systematic investigation of gridding-related scaling effects on annual statistics of daily temperature and precipitation maxima: a case study for south-east Australia. Weather Clim Extremes 9:6–16. https://doi.org/10.1016/j.wace.2015.06.003

Azorin-Molina C, Guijarro JA, McVicar TR, Frost BCT, Chen D (2019) An approach to homogenize daily peak wind gusts: an application to the Australian series. Int J Climatol 39:2260–2277. https://doi.org/10.1002/joc.5949

Curio J, Scherer D (2016) Seasonality and spatial variability of dynamic precipitation controls on the Tibetan plateau. Earth Syst Dyn 7:767–782. https://doi.org/10.5194/esd-7-767-2016

Curio J, Maussion F, Scherer D (2015) A 12-year high-resolution climatology of atmospheric water transport over the Tibetan plateau. Earth Syst Dynam 6:109–124. https://doi.org/10.5194/esd-6-109-2015

Dee DP, Uppala SM, Simmons AJ, Berrisford P, Poli P, Kobayashi S et al (2011) The ERA-Interim reanalysis: configuration and performance of the data assimilation system. Q J R Meteorol Soc 137:553–597. https://doi.org/10.1002/qj.828

Dong Z, Hu G, Qian G, Lu J, Zhang Z, Luo W, Lyu P (2017) High-altitude Aeolian research on the Tibetan plateau. Rev Geophys 55:864–901. https://doi.org/10.1002/2017RG000585

Duan A, Xiao Z (2015) Does the climate warming hiatus exist over the Tibetan plateau? Sci Rep 5:13711. https://doi.org/10.1038/srep13711

Dunn RJH, Willet KM, Thorne PW, Woolley EV, Durre I, Dai A et al (2012) HadISD: a quality-controlled global synoptic report database for selected variables at long-term stations from 1973–2011. Clim past 8:1649–1679. https://doi.org/10.5194/cp-8-1649-2012

Dunn RJH, Willet KM, Morice CP, Parker DE (2014) Pairwise homogeneity assessment of HadISD. Clim past 10:1501–1522. https://doi.org/10.5194/cp-10-1501-2014

Dunn RJH, Willet KM, Parker DE, Mitchell L (2016) Expanding HadISD: quality-controlled, sub-daily station data from 1931. Geosci Instrum Methods and Data Syst 5:473–491. https://doi.org/10.5194/gi-5-473-2016

Dunn RJH (2019) HadISD version 3: monthly updates. Met Office Hadley Centre Technical Notes. https://digital.nmla.metoffice.gov.uk/digitalFile_13890750-fb6f-42c7-92df-1c4504621fae/ Accessed 7 Aug 2023

Gao Y-X, Tang M-C, Luo S-W, Shen Z-B, Li C (1981) Some aspects of recent research on the Qinghai-Xizang plateau meteorology. Bull Am Meteorol Soc 62:31–35. https://doi.org/10.1175/1520-0477(1981)062%3c0031:SAORRO%3e2.0.CO;2

Gao Y, Xu J, Chen D (2015) Evaluation of WRF mesoscale climate simulations over the Tibetan plateau during 1979–2011. J Clim 28:2823–2841. https://doi.org/10.1175/JCLI-D-14-00300.1

Gesch DB, Verdin KL, Greenlee SK (1999) New land surface digital elevation model covers the Earth. Eos Transact Am Geophys Union 80:69–70

Giorgi F, Shields C (1999) Tests of precipitation parametrizations availvle in the latest version of NCAR regional climate model (RegCM) over continental United States. J Geophys Res Atmos 104:6353–6375. https://doi.org/10.1029/98JD01164

Gomis-Cebolla J, Rattayova V, Salazar-Galán S, Francés F (2023) Evaluation of ERA5 and ERA5-Land reanalysis precipitation datasets over Spain (1951–2020). Atmos Res 284:106606. https://doi.org/10.1016/j.atmosres.2023.106606

Grell GA (1993) Prognostic evaluation of assumptions used by cumulus parameterization. Mon Weather Rev 121:764–787. https://doi.org/10.1175/1520-0493(1993)121%3c0764:PEOAUB%3e2.0.CO;2

Grell GA, Dévényi D (2002) A generalized approach to parameterizing convection combining ensemble and data assimilation techniques. Geophys Res Lett 29:1–4. https://doi.org/10.1029/2002GL015311

Guijarro JA (2018) Homogenization of climatic series with Climatol. www.climatol.eu/homog_climatol-en.pdf Accessed 7 Aug 2023

Helbig N, Mott R, van Herwijnen A, Winstral A, Jonas T (2017) Parameterizing surface wind speed over complex topography. J Geophys Res Atmos 122:651–667. https://doi.org/10.1002/2016JD025593

Hersbach H, de Rosnay P, Bell B, Schepers D, Simmons A, Soci C et al (2018) Operational global reanalysis: progress, future directions and synergies with NWP. ERA Report Series. https://www.ecmwf.int/node/18765 Accessed 7 Aug 2023

Hong S-Y, Noh Y, Dudhia J (2006) A new vertical diffusion package with an explicit treatment of entrainment processes. Mon Weather Rev 134:2318–2341. https://doi.org/10.1175/MWRR3199.1

IPCC (2019) IPCC special report on the ocean and cryosphere in a changing climate. Cambridge Press, Cambridge

Janjić ZI (1994) The step-mountain eta coordinate model: Further developments of the convection, viscous sublayer, and turbulence closure schemes. Mon Weather Rev 122:927–945. https://doi.org/10.1175/1520-0493(1994)122%3c0927:TSMECM%3e2.0.CO;2

Jiménez PA, Dudhia J (2012) Improving the representation of resolved and unresolved topographic effects on surface wind in the WRF model. J Appl Meteor Climatol 51:300–316. https://doi.org/10.1175/JAMC-D-11-084.1

Jiménez PA, González-Rouco JF, García-Bustamante E, Navarro J, Montávez JP, Vilà-Guerau de Arellano J et al (2010) Surface wind regionalization over complex terrain: Evaluation and analysis of a high-resolution WRF simulation. J Appl Meteorol Climatol 49:268–287. https://doi.org/10.1175/2009JAMC2175.1

Kang S, Xu Y, You Q, Flügel W-A, Pepin N, Yao T (2010) Review of climate and cryospheric change in the Tibetan Plateau. Environ Res Lett 5:015101. https://doi.org/10.1088/1748-9326/5/1/015101

Kim Y, Evans JP, Sharma A (2023) Multivariate bias correction of regional climate model boundary conditions. Clim Dyn. https://doi.org/10.1007/s00382-023-06718-6

Kukulies J, Lai H-W, Curio J, Feng Z, Lin C, Li P et al (2023) Mesoscale convective systems in the third pole region: Characteristics, mechanisms and impact on precipitation. Front Earth Sci 11:1143380. https://doi.org/10.3389/feart.2023.1143380

Kunz M, Mohr S, Rauthe M, Lux R, Kottmeier C (2010) Assessment of extreme wind speeds from Regional Climate Models – Part 1: Estimation of return values and their evaluation. Nat Hazards Earth Syst Sci 10:907–922. https://doi.org/10.5194/nhess-10-907-2010

Landberg L (2016) Meteorology for wind energy an introduction. John Wiley & Sons Ltd, Chichester

Li X, Gao Y, Pan Y, Xu Y (2017) Evaluation of near-surface wind speed simulations over the Tibetan Plateau from three dynamical downscalings based on WRF model. Theor Appl Climatol 134:1399–1411. https://doi.org/10.1007/s00704-017-2353-9

Li P, Furtado K, Zhou T, Chen H, Li J, Guo Z, Xiao C (2018) The diurnal cycle of East Asian summer monsoon precipitation simulated by the Met Office Unified Model at convection-permitting scales. Clim Dyn 55:131–151. https://doi.org/10.1007/s00382-018-4368-z

Li P, Furtado K, Zhou T, Chen H, Li J (2021a) Convection-permitting modelling improves simulated precipitation over the central and eastern Tibetan Plateau. Q J R Meteorol Soc 147:341–362. https://doi.org/10.1002/qj.3921

Li Z, Xiao Z-N, Zheng C-W (2021b) Observation analysis of wind climate in China for 1971–2017 under the demand of wind energy evaluation and utilization. Energy Rep 7:3535–3546. https://doi.org/10.1016/j.egyr.2021.06.012

Lin C, Chen D, Yang K, Ou T (2018) Impact of model resolution on simulating the water vapor transport through the central Himalayas: implication for models' wet bias over the Tibetan Plateau. Clim Dyn 51:3195–3207. https://doi.org/10.1007/s00382-018-4074-x

Liu X, Bai A, Liu C (2009) Diurnal variations of summertime precipitation over the Tibetan Plateau in relation to orographically-induced regional circulations. Environ Res Lett 4:045203. https://doi.org/10.1088/1748-9326/4/4/045203

Ma Y, Hu Z, Xie Z, Ma W, Wang B, Chen X et al (2020) A long-term (2005–2016) dataset of hourly integrated land-atmosphere interaction observations on the Tibetan plateau. Earth Syst Sci Data 12:2937–2957. https://doi.org/10.5194/essd-12-2937-2020

Maussion F, Scherer D, Finkelnburg R, Richters J, Yang W, Yao T (2011) WRF simulation of a precipitation event over the Tibetan Plateau, China – an assessment using remote sensing

and ground observations. Hydrol Earth Syst Sci 15:1795–1817. https://doi.org/10.5194/hess-15-1795-2011

Maussion F, Scherer D, Mölg T, Collier E, Curio J, Finkelnburg R (2014) Precipitation seasonality and variability over the Tibetan plateau as resolved by the High Asia reanalysis. J Climate 27:1910–1927. https://doi.org/10.1175/JCLI-D-13-00282.1

McVicar TR, Van Niel TG, Li LT, Hutchinson MF, Mu XM, Liu ZH (2007) Spatially distributing monthly reference evapotranspiration and pan evaporation considering topographic influences. J Hydrol 338:196–220. https://doi.org/10.1016/j.hydrol.2007.02.018

Miao H, Dong D, Huang G, Hu K, Tian Q, Gong Y (2020) Evaluation of northern hemisphere surface wind speed and wind power density in multiple reanalysis datasets. Energy 200:117382. https://doi.org/10.1016/j.energy.2020.117382

Miller CA, Davenport AG (1998) Guidelines for the calculation of wind speed-ups in complex terrain. J Wind Eng Ind Aerodyn 74–76:189–197. https://doi.org/10.1016/S0167-6105(98)00016-6

Minola L, Zhang F, Azorin-Molina C, Safaei Pirooz AA, Flay RGJ, Hersbach H et al (2020) Near-surface mean and gust wind speeds in ERA5 across Sweden: towards an improved gust parametrization. Clim Dyn 55:887–907

Minola L, Azorin-Molina C, Guijarro JA, Zhang G, Son S-W, Chen D (2021a) Climatology of near-surface daily peak wind gusts across Scandinavia: Observations and model simulations. J Geophys Res Atmos. 126:033534. https://doi.org/10.1029/2020JD033534

Minola L, Reese H, Lai H-W, Azorin-Molina C, Guijarro JA, Son S-W et al (2021b) Wind stilling-reversal across Sweden: The impact of land-use and large-scale atmospheric circulation changes. Int J Climatol 42:1049–1071. https://doi.org/10.1002/joc.7289

Muñoz-Sabater J, Dutra E, Agustí-Panareda A, Albergel C, Arduini G, Balsamo G et al: ERA5-Land: a state-of-the-art global reanalysis dataset for land applications. Earth Syst Sci Data 13:4349–4383. https://doi.org/10.5194/essd-13-4349-2021

Ou T, Chen D, Chen X, Lin C, Yang C, Lai H-W et al (2020) Simulation of summer precipitation diurnal cycles over the Tibetan Plateau at the gray-zone grid spacing for cumulus parametrization. Clim Dyn 54:3525–3539. https://doi.org/10.1007/s00382-020-05181-x

Ou T, Chen D, Tang J, Lin C, Wang X, Kukulies J, Lai H-W (2023) Wet bias of summer precipitation in the northwestern Tibetan Plateau in ERA5 is linked to overestimated lower-level southerly wind over the plateau. Clim Dyn. https://doi.org/10.1007/s00382-023-06672-3

R Core Team (2020) R: A language and environment for statistical computing. R Fundation for Statistical Computing. https://www.R-project.org/ Accessed 7 Aug 2023

Ramon J, Lledó L, Torralba V, Soret A, Doblas-Reyes FJ (2019) What global reanalysis best represents near-surface winds? Q J R Meteorol Soc 145:3236–3251. https://doi.org/10.1002/qj.3616

Rotach MW, Gohm A, Lang MN, Leukauf D, Stiperski I, Wagner JS (2015) On the vertical exchange of heat, mass, and momentum over complex, mountainous terrain. Front Earth Sci 3:76. https://doi.org/10.3389/feart.2015.00076

Serafin S, Adler B, Cuxart J, De Wekker SFJ, Gohm A, Grisogono B et al (2018) Exchange processes in the atmospheric boundary layer over mountainous terrain. Atmos 9:102. https://doi.org/10.3390/atmos9030102

Shi P, Zhang G, Kong F, Chen D, Azorin-Molina C, Guijarro JA (2019) Variability of winter haze over the Beijing-Tianjin-Hebei region tied to wind speed in the lower troposphere and particulate sources. Atmos Res 215:1–11. https://doi.org/10.1016/j.atmosres.2018.08.013

Skamarock WC, Klemp JC, Dudhia J, Gill DO, Barker DM, Duda MG et al (2008) A description of the advanced research WRF version 3 NCAR Technical note (NCAR/TN-475+STR). Doi: https://doi.org/10.5065/D68S4MVH Accessed 7 Aug 2023

Smith A, Lott N, Vose R (2011) The integrated surface database: recent developments and partnerships. Bull Am Meteorol Soc 92:704–708. https://doi.org/10.1175/2011BAMS3015.1

Sun H, Su F, He Z, Ou T, Chen D, Li Z et al (2021) Hydrological evaluation of high-resolution precipitation estimates from The WRF model in the third pole river basins. J Hydrometeorol 22:2055–2071. https://doi.org/10.1175/JHM-D-20-0271.1

Wan H, Wang XL, Swail VR (2010) Homogenization and trend analysis of Canadian near-surface wind speeds. J Clim 23:1209–1225. https://doi.org/10.1175/2009JCLI3200.1

Wang X, Tolksdorf V, Otto M, Scherer D (2020) WRF-based dynamical downscaling of ERA5 reanalysis data for High Mountain Asia: towards a new version of the High Asia Refined analysis. In J Climatol 41:743–762. https://doi.org/10.1002/joc.6686

Whiteman CD (2000) Mountain meteorology: Fundamentals and application. Oxford University Press, Oxford

Wilks DS (1995) Statistical methods in the atmospheric sciences. Academic Press, San Diego

Wohland J, Omrani N-E, Witthaut D, Keenlyside NS (2019) Inconsistent wind speed trends in current twentieth Century Reanalyses. J Geophys Res Atmos 124:1931–1940. https://doi.org/10.1029/2018JD030083

Wood N (2000) Wind flow over complex terrain: a historical perspective and the prospect for large-eddy modelling. Bound-Layer Meteorol 96:11–32. https://doi.org/10.1023/A:1002017732694

Yang K, Koike T, Fujii H, Tamura T, Xu X, Bian L et al (2004) The daytime evolution of the atmospheric boundary layer and convection over the Tibetan Plateau: Observations and simulation. J Meteorol Soc Jpn 82:1777–1792. https://doi.org/10.2151/jmsj.82.1777

Yang K, Wu H, Qin J, Lin C, Tang W, Chen Y (2014) Recent climate changes over the Tibetan Plateau and their impacts on energy and water cycle: A review. Glob Planet Change 112:79–91. https://doi.org/10.1016/j.gloplacha.2013.12.001

Yao T, Thompson LG, Mosbrugger V, Zhang F, Ma Y, Luo T et al (2012) Third Pole Environment. Environ Dev 3:52–64. https://doi.org/10.1016/j.envdev.2012.04.002

Yao Z, Li X, Xiao J (2018) Characteristics of daily extreme wind gusts on the Qinghai-Tibet plateau, China. J Arid Land 10:673–685. https://doi.org/10.1007/s40333-018-0094-y

Yin A, Dang Y-Q, Zhang M, Chen X-H, McRivette MW (2008) Cenozoic tectonic evolution of the Qaidam basin and its surrounding regions (Part 3): Structural geology, sedimentation, and regional tectonic reconstruction. Geol Soc Am Bull 120:847–876. https://doi.org/10.1130/B26232.1

You Q, Fraedrich K, Min J, Kang S, Zhu X, Pepin N et al (2014) Observed surface wind speed in the Tibetan Plateau since 1980 and its physical causes. In J Climatol 34:1873–1882. https://doi.org/10.1002/joc.3807

Zhang G, Azorin-Molina C, Chen D, Guijarro JA, Kong F, Minola L et al (2020) Variability of daily maximum wind speed across China, 1975–2016. J Clim 33:2793–2816. https://doi.org/10.1175/JCLI-D-19-0603.1

Zhao Y, Li J, Zhang Q, Jiang X, Feng A (2019) Diurnal variations in surface wind over the Tibetan Plateau. Atmos 10:112. https://doi.org/10.3390/atmos10030112

Zheng H, Liu X, Liu C, Dai X, Zhu R (2009) Assessing contributions to panevaporation trends in Haihe River Basin. China J Geophys Res Atmos 114:D24105. https://doi.org/10.1029/2009JD012203

Zhou X, Beljaars A, Wang Y, Huang B, Lin C, Chen Y et al (2017) Evaluation of WRF simulations with different selections of subgrid orographic drag over the Tibetan Plateau. J Geophys Res Atmos 122:9759–9772. https://doi.org/10.1002/2017JD027212

Zhou X, Yang K, Wang Y (2018) Implementation of a turbulent orographic form drag scheme in WRF and its application to the Tibetan Plateau. Clim Dyn 50:2443–2455. https://doi.org/10.1007/s00382-017-3677-y